CHALMERS
UNIVERSITY OF TECHNOLOGY

Wind-induced sound source mapping on Volvo V70

Master's thesis in Automotive Engineering

Zhang Ze

Department of Applied Mechanics
CHALMERS UNIVERSITY OF TECHNOLOGY
Gothenburg, Sweden 2015

MASTER'S THESIS IN AUTOMOTIVE ENGINEERING

Wind-induced sound source mapping on Volvo V70

Zhang Ze

Department of Applied Mechanics
Division of Vehicle Engineering and Autonomous Systems
CHALMERS UNIVERSITY OF TECHNOLOGY
Göteborg, Sweden 2015

Wind-induced sound source mapping on Volvo V70

Zhang Ze

Master Thesis 2015:36
ISSN 1652-8557
Department of Applied Mechanics
Division of Vehicle Engineering and Autonomous Systems
Chalmers University of Technology
SE-412 96 Göteborg
Sweden
Telephone: + 46 (0)31-772 1000

Cover:
A Volvo V70 ready to be tested at Volvo Wind tunnel

Name of the printers / Department of Applied Mechanics
Göteborg, Sweden 2015-06-08

Wind-induced sound source mapping on Volvo V70

Master thesis in Automotive Engineering
Zhang Ze
Department of Applied Mechanics
Division of Vehicle Engineering and Autonomous Systems
Chalmers University of Technology

Abstract

The project is aimed to gain a better understanding of the possibilities and limitations of various sound source measuring technologies including beamforming and Equivalent Source Method (ESM) in aerodynamic noise measurement on a car. It was shown that ESM method has a better resolution for sound source localization at low frequencies and recommended to use for the next coming projects. Subsequently tools like intensity probe and 3D acoustic camera that use aforementioned technologies are then utilized to identify and analyse sound source both inside and outside a Volvo V70. Various configurations with changes at the regions of interests have been tested out, some of which are A-post, rear view mirror, cowl cavity, etc. Afterwards the results are postprocessed, analysed and compared with CFD simulations from Ansys Fluent. Furthermore, a coherence analysis between exterior sound and interior sound is conducted and most influential exterior sound source to the inside noise level is determined. It was shown that mid to low frequency noise sources are the main contributors to interior noise. The low frequency noise is caused by wheelhouse and air flushing on the side window from rear view mirror. The mid frequency noise is from A-post and cowl cavity.

Key words: sound source mapping, sound source visualization, beamforming, equivalent source method, coherence analysis, car exterior sound, car interior sound, aerodynamic noise, side view mirror, A-post.

Contents

Preface

In this study, studies regarding interior and exterior noise of a Volvo V70 have been done with intensity probe, CFD simulation and 3D acoustic camera. The tests have been carried out from January 2015 to June 2015. The work is a part of research project at Volvo Cars NVH Center, Sweden.

This project has been carried out with Olga Roditcheva as supervisor at Volvo and Professor Lennart Löfdahl as the examiner. All tests have been carried out at Volvo Wind tunnel and preparation room at Volvo Torslanda. My supervisor Olga Rodicheva is highly appreciated for her help with planning the test. I would also like to thank LMS Siemens for their support and involvement.

Finally, it should be noted that the tests could never have been conducted without the sense of high quality and professionalism of the laboratory staff.

Göteborg 2015-06-08

Zhang Ze

Notations

Roman upper case letters

I	Sound intensity
$IM\ G_{AB}$	Cross spectrum of signals from two channels
K	Total number of equivalent sources
P	Sound pressure at target point
$P_1 - P_2$	Difference in pressure between two microphones
R_{mk}	Distance between the k^{th} equivalent source and l^{th} measurement point
V	Particle velocity

Roman lower case letters

c	Local sound speed
d	Width of intensity probe spacer
$g(R_{mk}, t)$	The impulsive response function between k^{th} equivalent source and m^{th} measurement point
l	Distance from microphone array to the measuring spot
$p_m(t)$	Pressure at m^{th} measurement point
$\frac{\partial p}{\partial r}$	Pressure gradient
$q_k(t)$	k^{th} equivalent source strength at time t
$s(t)$	Calculated average signal
$s_i(t)$	Signal from i^{th} microphone

Greek lower case letters

$\delta(t)$	Dirac Delta function
θ	Angle between the sound wave and microphones plane
ρ	Air density
τ_j	Calculated delay time (phase shift)
τ_{mk}	Retarded time
ω	Angular frequency

Others

$*$	Convolution sign

1 Introduction

With ever increasingly strict regulations and customer expectations, more emphasis than ever has been put on automobile noise. Automobile noise can be categorized into three groups in terms of the location of the source – drive train noise, which is from the engine and transmission; road noise, which is from the suspension due to the irregularities of the road and wind induced noise, which is from airflow in and around the car.

For drivetrain noise and road noise, a large amount of work has been done which focus on noise generation mechanism and analysis of sound transfer path from sound source location to compartment.

However, little work has been completed for similar issues on the wind-induced noise because of the complexity of the problem. Current work focus on either outside, i.e. how shape on one component will influence the sound intensity in the vicinity or inside, i.e. how wind-induced noise related compartment noise distribute over frequency. Little light has been shed on how compartment noise is influenced by exterior wind-induced noise or to rank, quantify that influence.

Given that compartment noise is due to exterior noise, it is crucial to investigate on the relationship between the outside wind-induced noise and inside compartment noise, which, once determined, could serve to improve compartment noise by modifying corresponding exterior component.

The aim and scope of the thesis project are listed below:

1) To better understand wind induced sound source outside and inside a Volvo V70
2) To pinpoint most influential outside sound source to the inside sound level
3) To recommend improvements on existing test methods
4) To understand better the testing equipment: field of application, limitation, etc.
5) To help decrease sound level in the compartment of a Volvo V70 and boost sales

2 Wind-induced Sound Sources around a Car

Following are background information about wind-induced noise on a car, professional readers may feel the need to skip this part and go directly to Chapter 3: exterior measurement.

Acoustic noise is the effect of rapid pressure changes transmitted as waves travelling at the speed of sound. Since interior noise has a great influence on occupant comfort, it's of great concern to the vehicle designer. Internal noise derives partly from internal sources such as ventilation system, and partly from the effects of external air flow, which is the main interest of this thesis project. Aerodynamic noise can also be categorized into boundary layer noise and edge noise. Boundary layer noise is generated by a turbulent boundary layer. A boundary layer noise on a car is usually high in frequency and can easily be damped out by the application of absorbent materials to the inside of body panel, thus it's not the major source. An edge noise is due to flow separation at sharp corners or the edge of styling details. It's usually distributed over a fairly narrow frequency band.

The main wind-induced sound sources around the car are shown in figure below. They include cowl cavity, front hood, rear view mirror, A-post, side window and trunk.

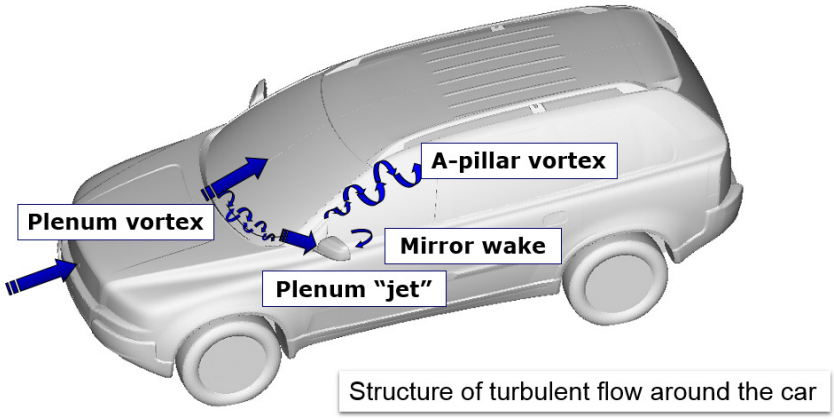

Figure 1: Structure of turbulent flow around the car.

3 Exterior Measurement

Sound intensity around car exterior is measured using intensity probe, through which major wind-induced sound sources outside are identified and ranked.
The experiment is conducted at Volvo wind tunnel (Fig. 2). It is equipped with 5-belt moving floor and boundary layer suction device that simulate the real flow under the car chassis under road condition. Slotted wall on each side can reduce undesirable turbulences in the wind tunnel. However, Volvo wind tunnel has little acoustic treatment, which increases the difficulty in measuring small noise contribution.

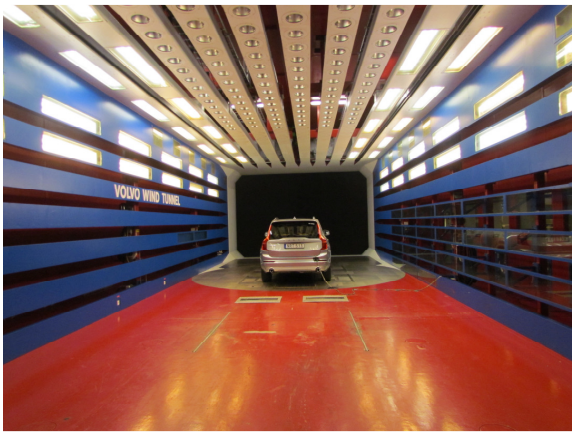

Figure 2: A Volvo V70 at Volvo wind tunnel.

3.1 Principle of intensity probe

An intensity probe that can measure the intensity level in a flow field is also utilized. Jacobsen (1991), Chung and Blaser (1981), Jacobsen and De Bree (2005) have thoroughly discussed the principle of this technique.

An intensity probe has two microphones with a spacer in between. Instead of measuring sound pressure using one single microphone, it can get the intensity information of the sound field by comparing signals from two channels. Intensity, energy flow rate through unit area, is a better indicator than pressure since it is more relevant to how large the noise is and is independent of environment because steady background noise will not be counted in intensity calculation. It is suitable for sound location, source ranking and noise mapping.

Two ways that can be used to calculate sound intensity are introduced below.

Algebraic method

$$I = P * V \tag{1}$$

Where

I is the intensity;
P is pressure at target point;
V is the particle velocity.

According to Euler's equation, the particle velocity can be calculated as in equation 2 below.

$$V = -\int \frac{1}{\rho}\frac{\partial p}{\partial r}dt \tag{2}$$

Where

$\frac{\partial p}{\partial r}$ is the pressure gradient,
ρ is air density.

For the sake of simplification, the pressure gradient is then replaced using finite difference approximation (Thompson and Tree (1981)) as investigated by Fahy (2002) like equation 3 below (see Jacobsen (2003)).

$$\frac{\partial p}{\partial r} \approx \frac{P_1 - P_2}{d} \tag{3}$$

Where

$P_1 - P_2$ is the difference of pressure between two microphones,
d is the spacer width.

In addition, the pressure is replaced with average pressure between two channels shown in equation 4 below.

$$P = \frac{P_1 + P_2}{2} \tag{4}$$

Thus, plug in everything, equation 5 can be obtained.

$$I = \frac{P_1 + P_2}{2d\rho}\int P_1 - P_2 dt \tag{5}$$

Fast Fourier Transform method

In FFT, following equation is used to calculate intensity.

$$I = -\frac{1}{\rho\omega d} IM\ G_{AB} \tag{6}$$

Where

ω is the angular frequency,
$IM\ G_{AB}$ is the imaginary part cross spectrum of signals of two channels.

The low frequency limit for the intensity probe is decided by the phase mismatch errors as discussed by Jacobsen (1993), since phase delay between two channels tend to become smaller when the frequency decrease, which, when small enough, will become undetectable by the instrument as shown in Fig. 3. For different space width, the lower limit could range from 60 Hz to 200 Hz.

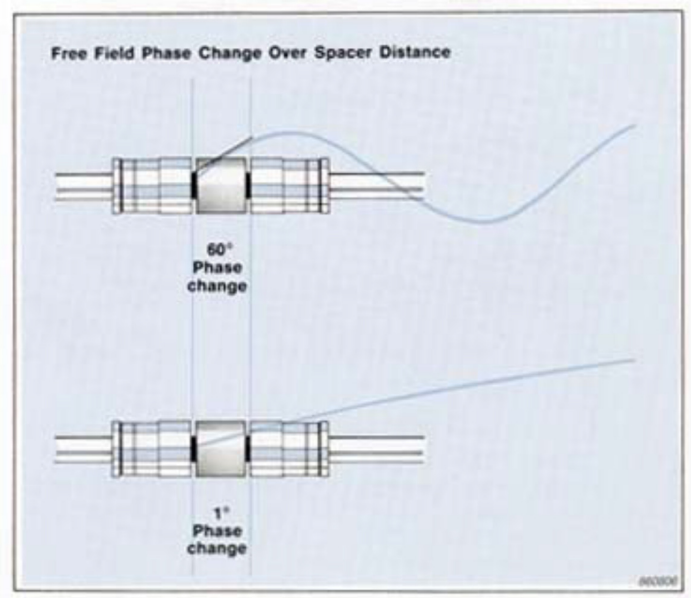

Figure 3: Low frequency limit of beamforming theory.

The high frequency limit is decided by differential approximation errors as discussed by Jacobsen, Cutanda and Juhl (1998) since it is the middle point between two microphones that is being measured, and once the frequency is too high, the gradient estimation would be inaccurate as shown in Fig. 4 below. For different spacer width, this value could vary from 1.25 KHz to 10 KHz.

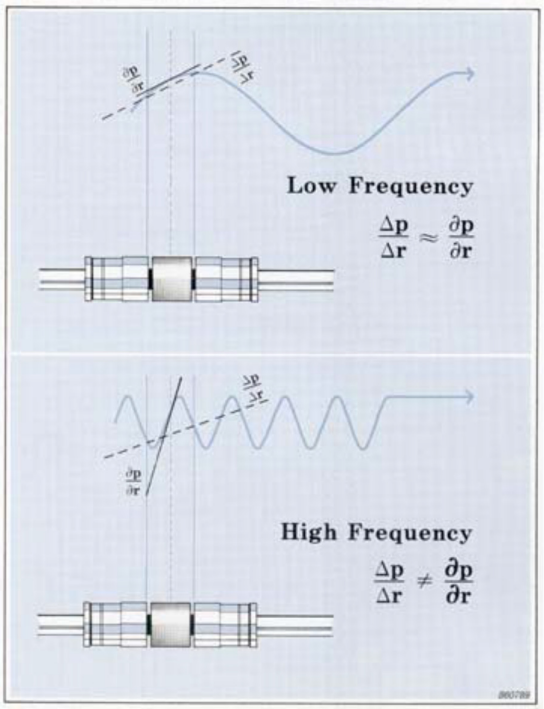

Figure 4: High frequency limit of beamforming theory.

Space with smaller width will favour the high frequency measuring and larger spacer width will favour low frequency measuring. That means spacer width will only shift the measuring range but not widen or narrow it.

3.2 Experiment setup

The experiment is conducted at Volvo wind tunnel. Instead of the common intensity probe that has two inline microphones that point to each other, the Volvo designed and manufactured intensity probe comprises two parallel microphones and seven DOFs. The reason is to obtain more accurate measurement in a high-speed flow field since the inline type probe would generate greater noise itself in a flow field due to the narrow gap between the two microphones, which may mask other noise that are more of interest. The tripod that holds the probe is magnetically fastened to the ground by an electromagnet. Fig. 5 below shows a detailed configuration.

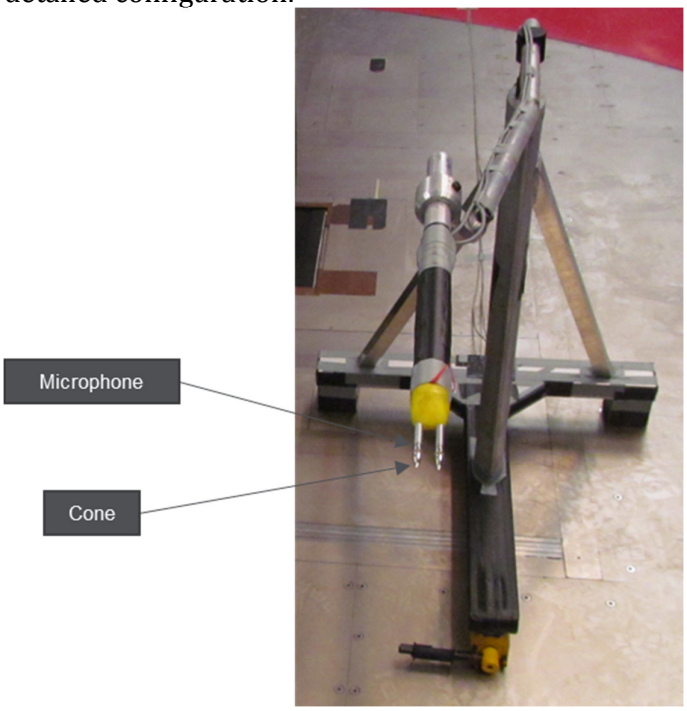

Figure 5: A detailed configuration of intensity probe used in this project.

In addition, to simulate the real road condition the rolling belt underneath the chassis is used. Sound intensity at seven locations is measured, including mirror (with BLIS), foot, hood grill, cowl and upper, middle and lower points at A-pillar. To make sound from cowl more substantial, wipers are removed. The test is conducted under three different speeds: 90 Km/h, 110 Km/h and 130 Km/h. Locations where measurements are taken are shown in Fig. 6 and 7.

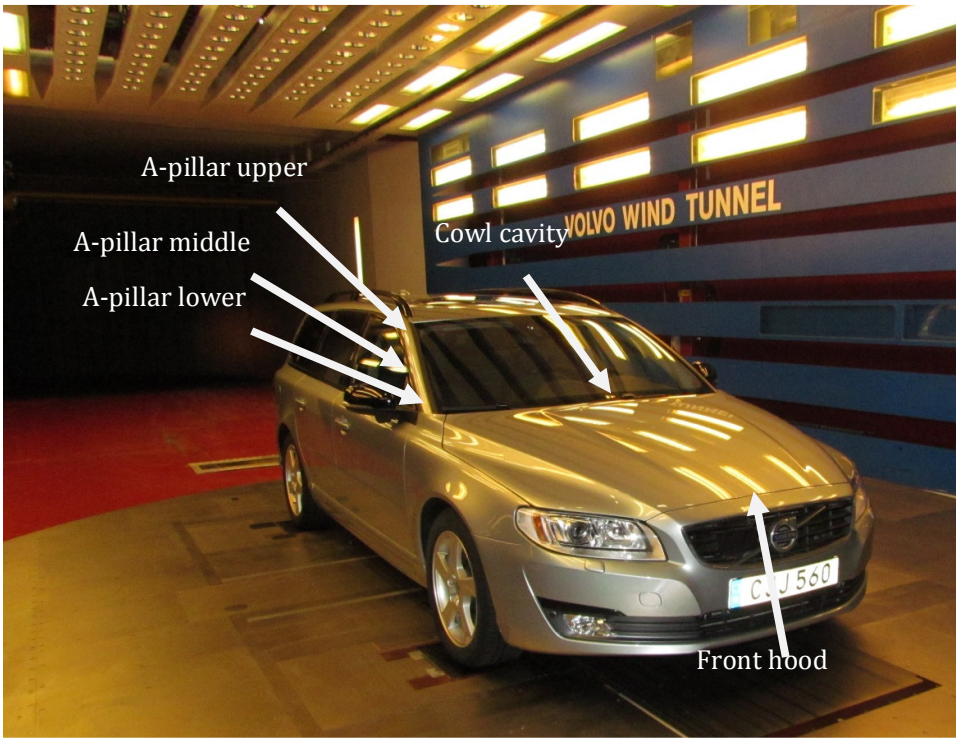

Figure 6: Locations for exterior measurement.

Figure 7: Locations for exterior measurement.

Care should be taken on the measuring location for mirror foot and mirror house. When measuring the intensity at mirror foot, the probe is placed directly next to mirror foot; however, to prevent the disturbance brought by the rear view mirror vortex, when measuring the intensity of rear view mirror, the probe is placed further away from rear view mirror.

3.3 Results

Pressure values gathered by the microphones are then converted to A-weighted sound intensity over frequency. Below are the maximum sound intensity level taken from the frequency spectrum (reference sound intensity 1 pW/m^2).

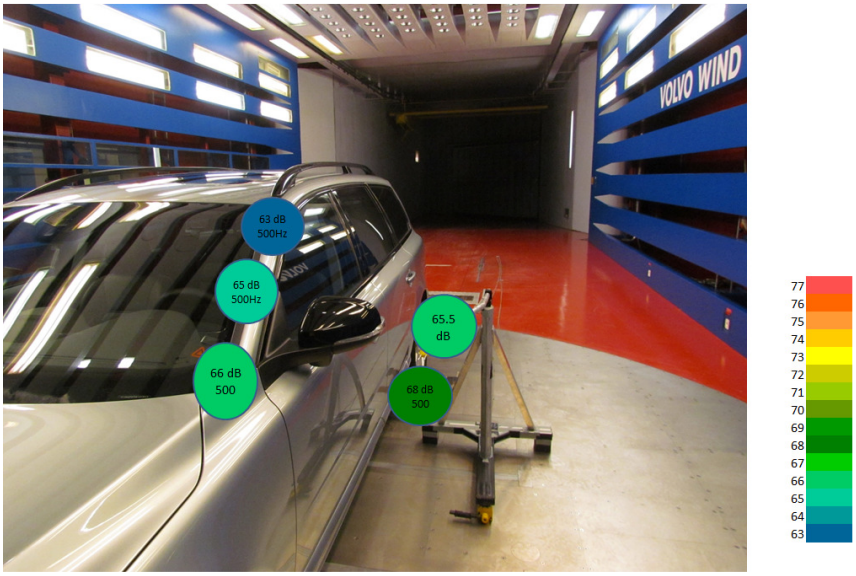

Figure 8: Maximum intensity at each measurement location at wind speed 90 km/h.

Figure 9: Maximum intensity at each measurement location at wind speed 110 km/h.

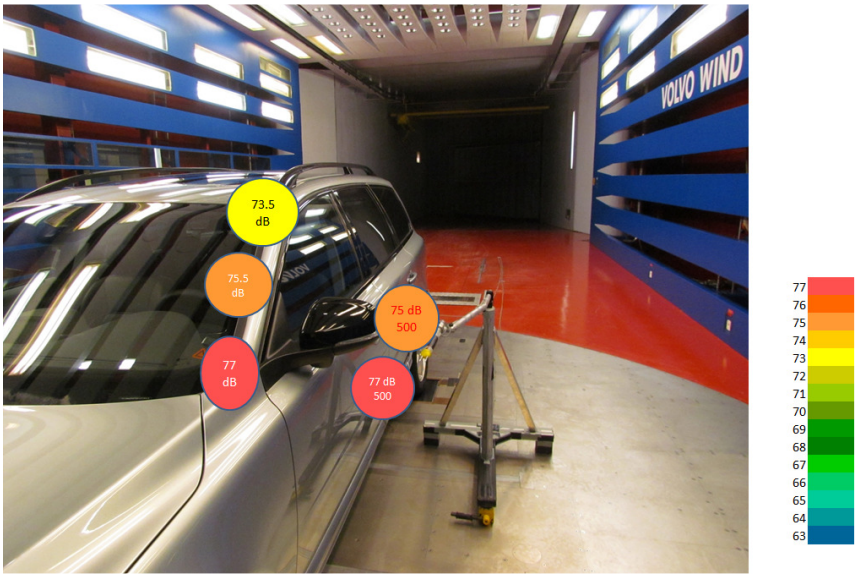

Figure 10: Maximum intensity at each measurement location at wind speed 130 km/h.

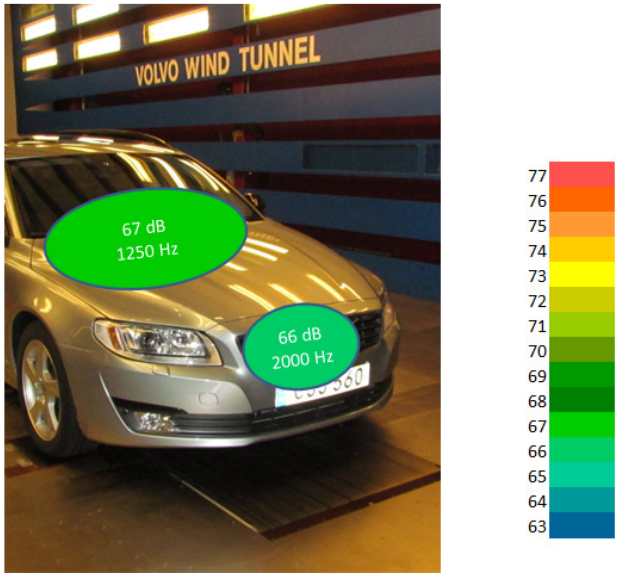

Figure 11: Maximum intensity at each measurement location at wind speed 90 km/h.

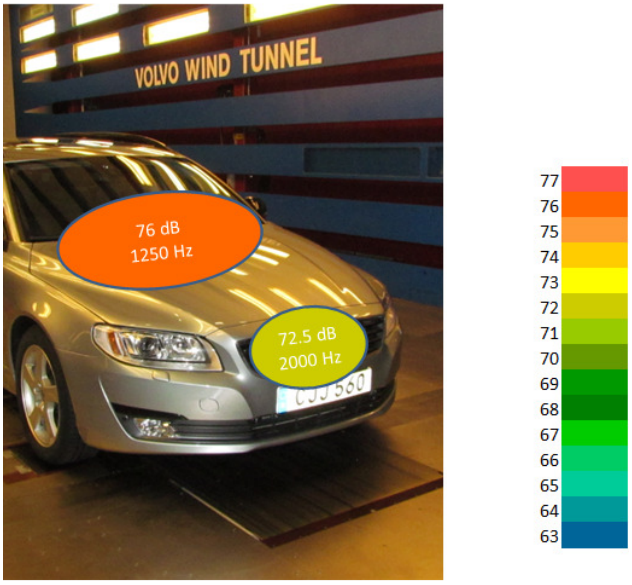

Figure 12: Maximum intensity at each measurement location at wind speed 110 km/h.

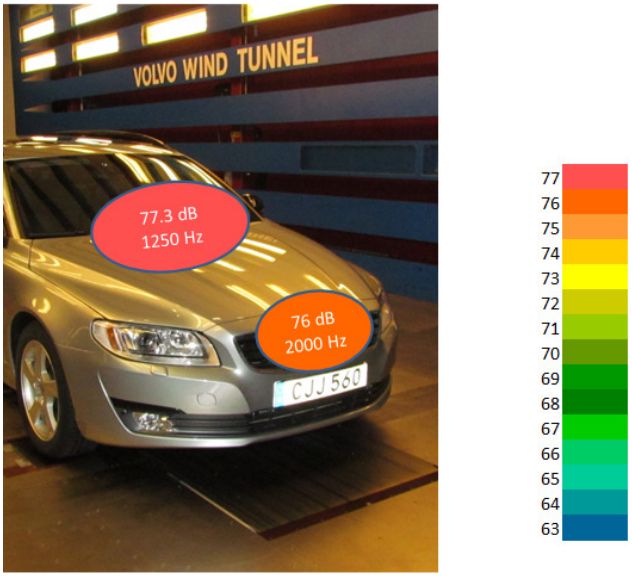

Figure 13: Maximum intensity at each measurement location at wind speed 130 km/h.

Based on these maximum intensity values at different locations, noise from different sources can be ranked as shown in Fig. 14.

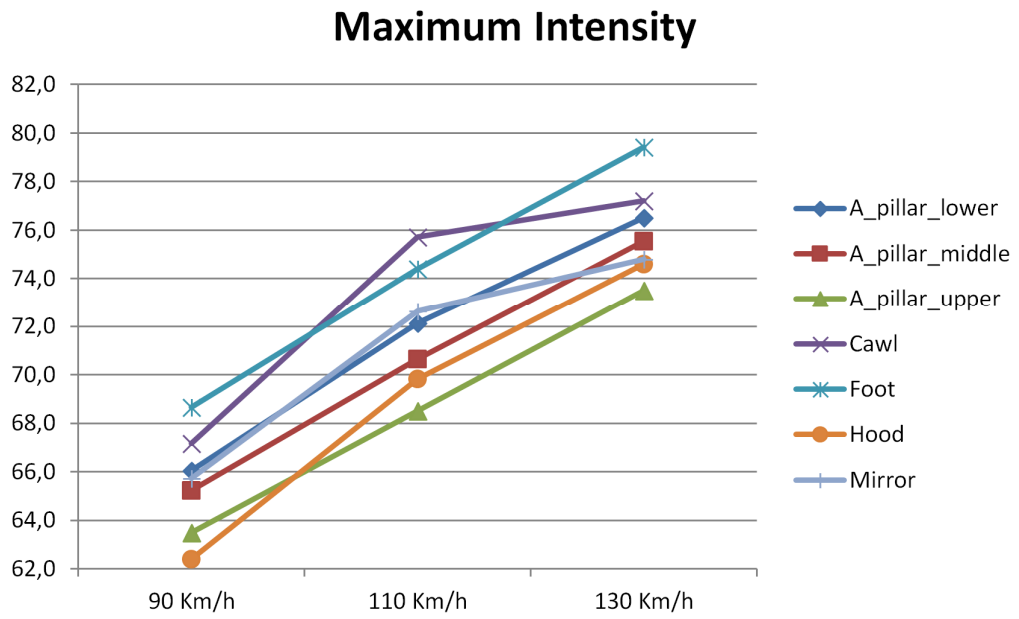

Figure 14: Maximum intensity for each component at different wind speed.

As can be seen from figure above, cowl cavity and mirror foot have the highest maximum sound intensity among measured regions, followed by mirror, A-pillar and hood.

If not the maximum intensity in the frequency spectrum is considered but the one value initial sound intensity in time domain computed using equation 7 indicated by Kinsler, Frey, Coppens and Sanders (1999), a similar figure can be obtained shown below.

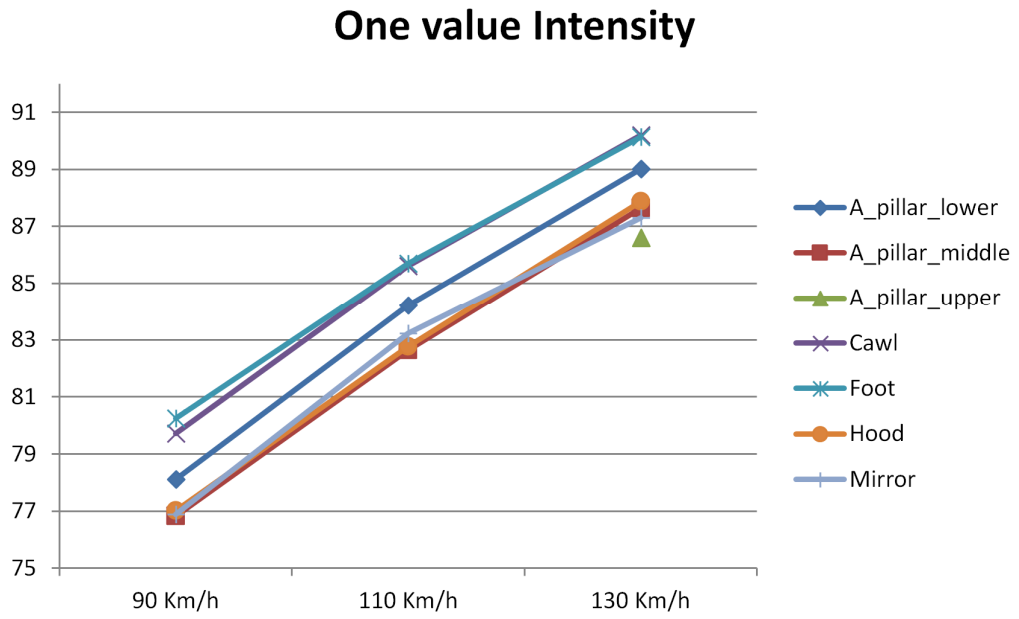

Figure 15: Average intensity at each measurement location at different wind speed.

$$I_{ini} = 10 * \log(\sum_{i=1}^{n} 10^{\frac{I_i}{10}}) \quad (7)$$

Where

I_i is the intensity level at one frequency band,
n is the total number of frequency bands,
I_{ini} is the one value intensity level generated.

3.4 Analysis

It is worth noticing that I_{ini} is not the exact initial intensity level because of A-weighting; however, a thorough examination reveals that A-weighting will not change the sign of inequality relation but only the quantity of difference itself.
One can clearly see that Fig. 16 follows the same trend as Fig. 17 that mirror foot and cowl cavity have the highest intensity value followed by A-pillar lower then followed by the hood, rear view mirror and the other two locations on A-pillar.
Contrary to one's expectation, the relationship between the intensity level and wind speed is neither linear nor convex. This can be explained by the logarithmic scale for the intensity level.

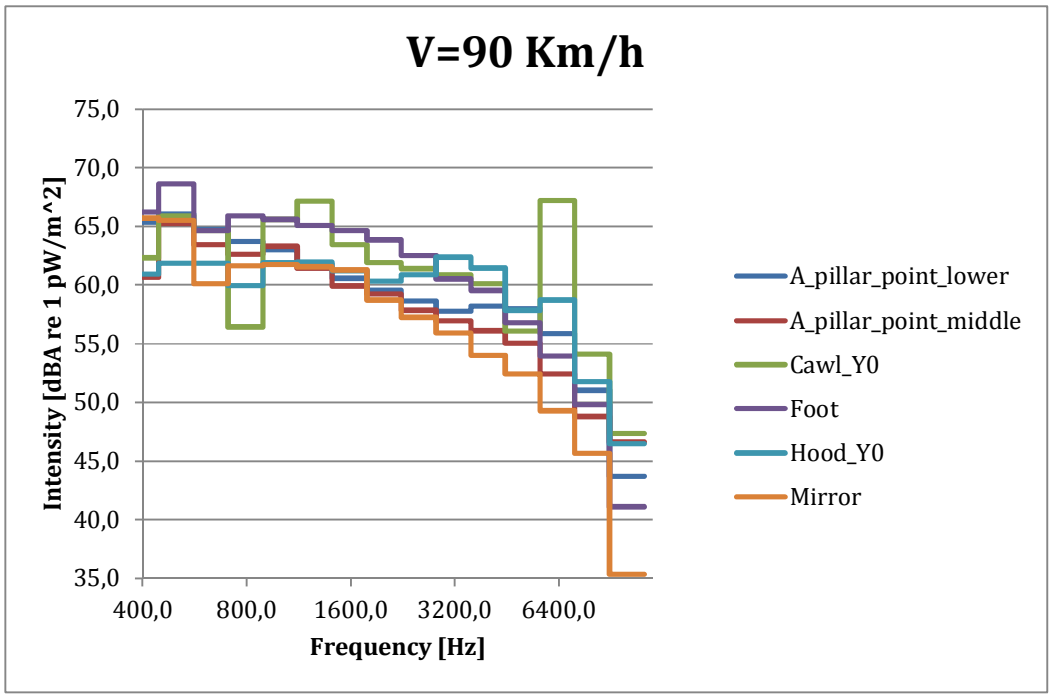

Figure 16: Sound intensity at each measurement locations at speed 90 Km/h.

At 90 Km/h wind speed, foot is dominating at the low frequency domain, the peak values of which appear at around 500 Hz, 1250 Hz; cowl is dominating at the high frequency domain, the frequencies where peak intensity values lies is around 6300 Hz. Mirror contributes the least.

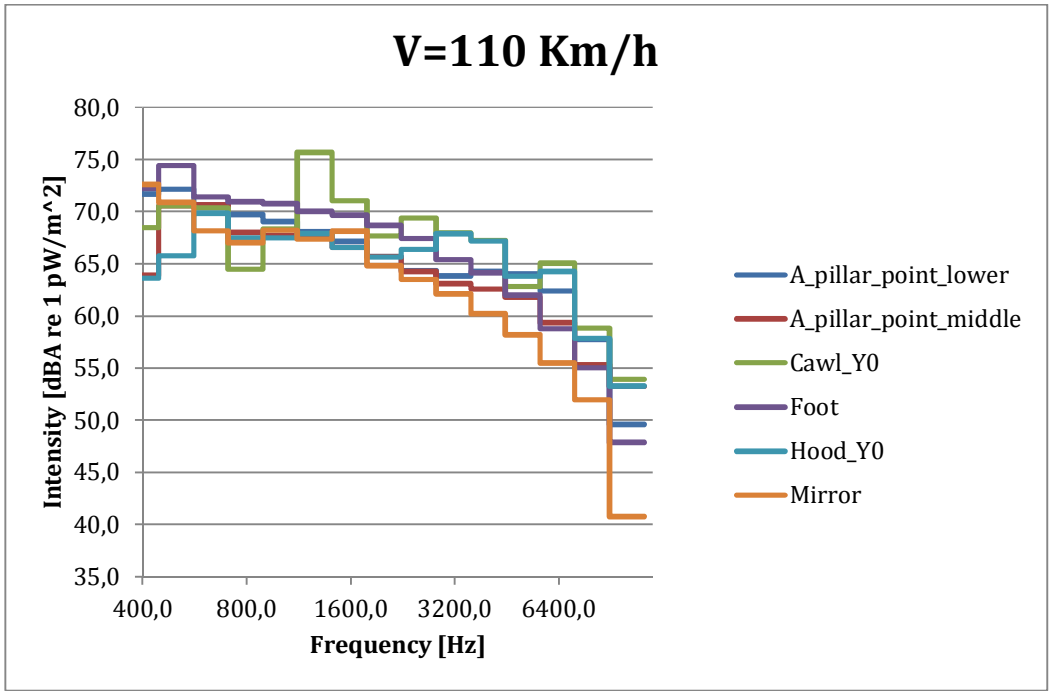

Figure 17: Sound intensity at each measurement locations at speed 110 Km/h.

At 110 Km/h wind speed, similar dominating pattern to that in 90 Km/h wind speed can be observed.

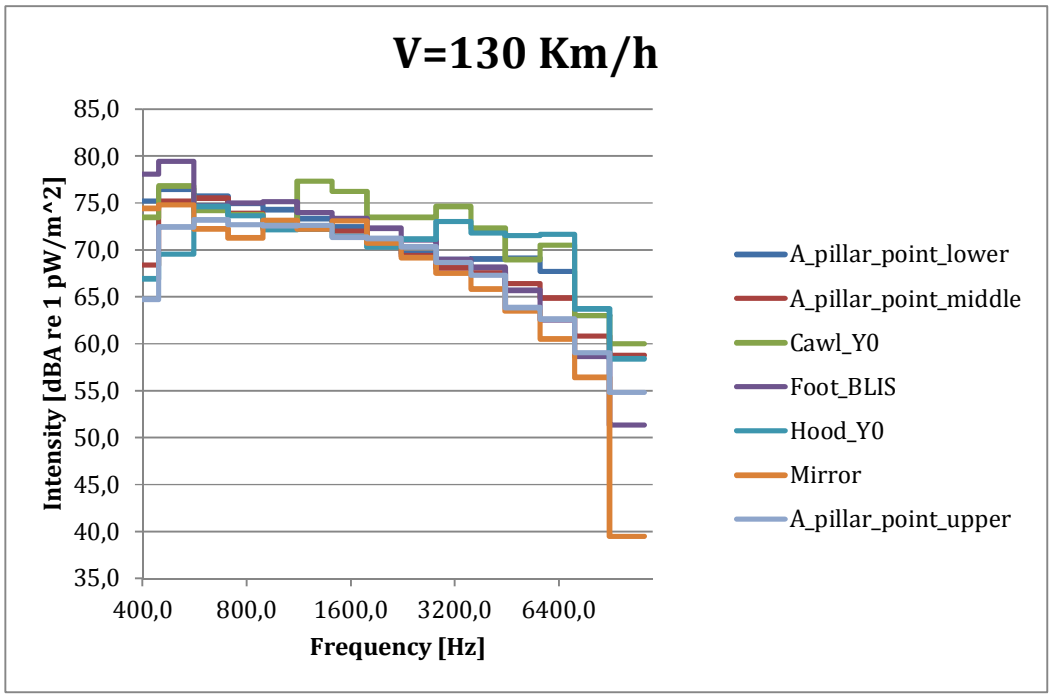

Figure 18: Sound intensity at each measurement locations at speed 130 Km/h.

At 130 Km/h wind speed, foot is still dominating at the low frequency domain, the peak values of which appear at around 500 Hz.

Following three figures are the intensity spectrum at A-pillar lower point, A-pillar middle point and mirror foot.

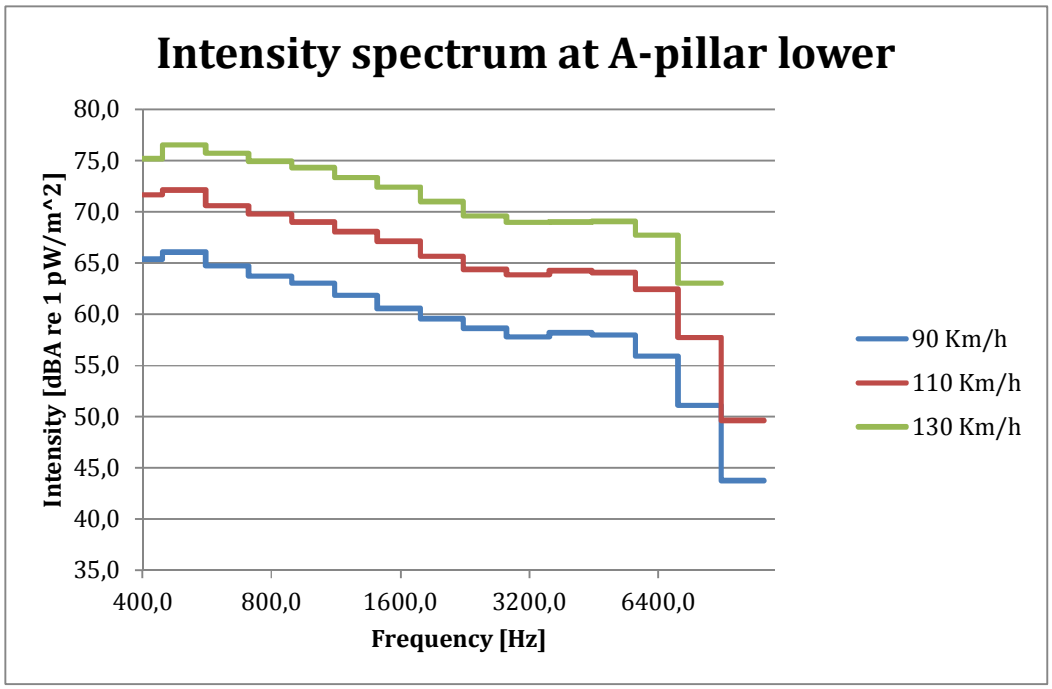

Figure 19: Sound intensity at A-pillar lower point at different wind speeds.

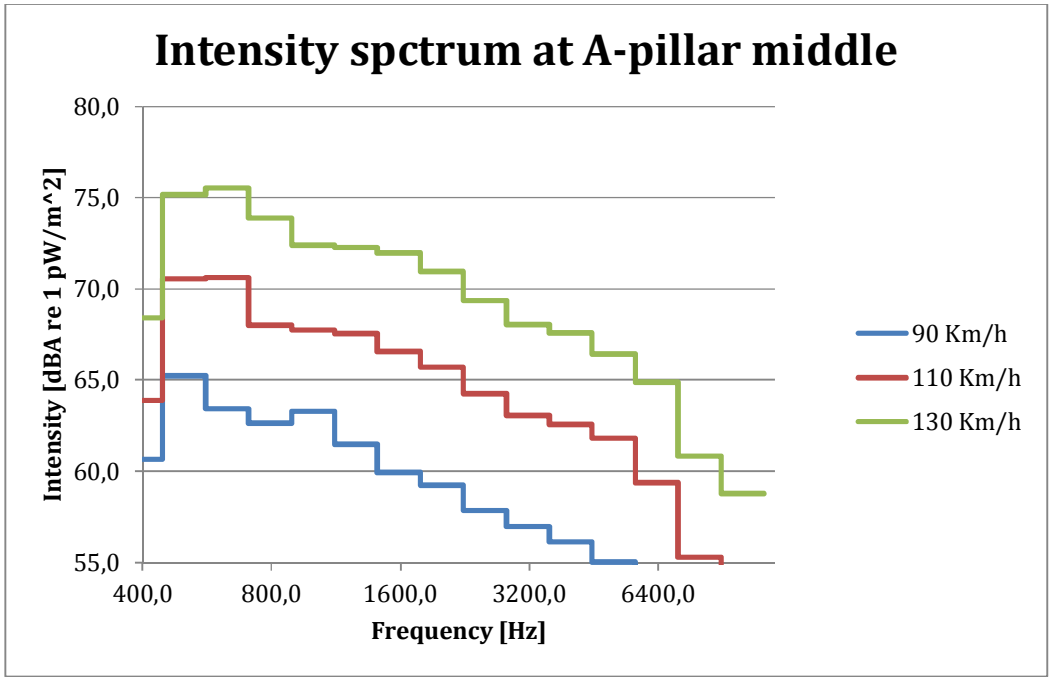

Figure 20: Sound intensity at A-pillar middle point at different wind speeds.

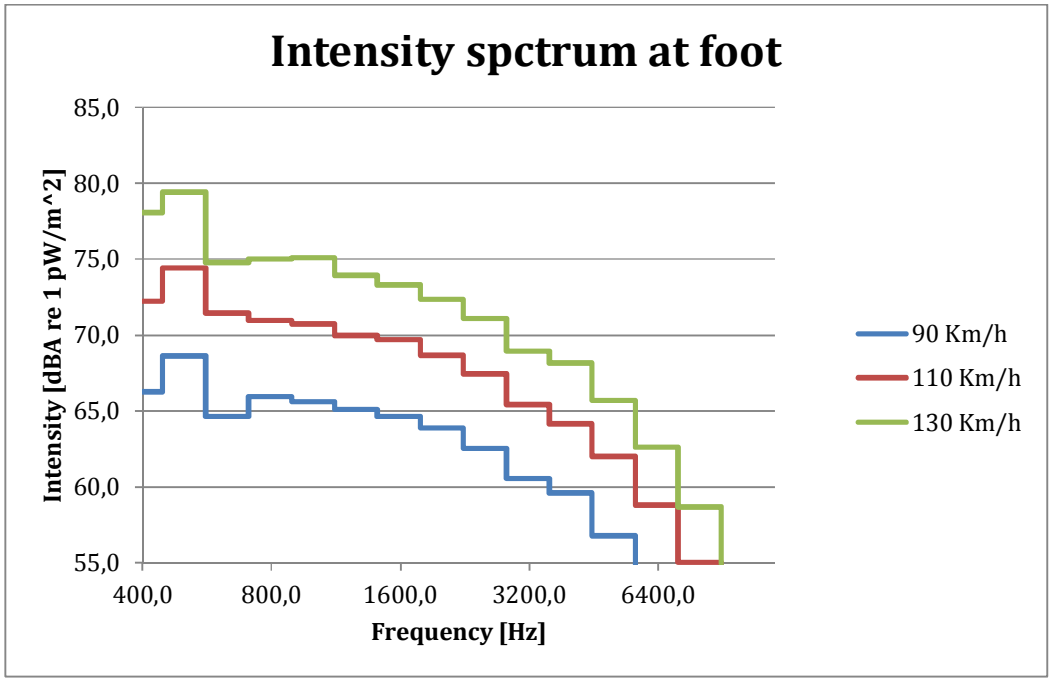

Figure 21: Sound intensity at mirror foot at different wind speeds.

It can be clearly seen that intensity increases with wind speed and wind speed will not affect the curve shape but only functions as a vertical shift to the curve. All peak values appear at around 500 Hz and there will be a 5 dB (A) shift with 20 Km/h wind speed difference.

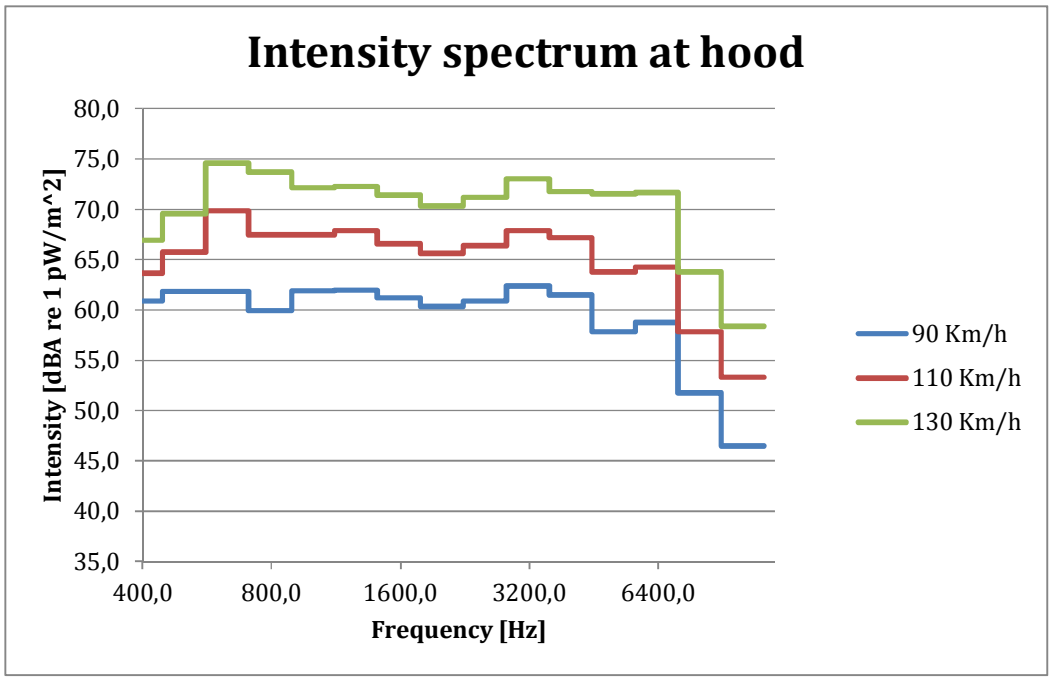

Figure 22: Sound intensity at hood at different wind speeds.

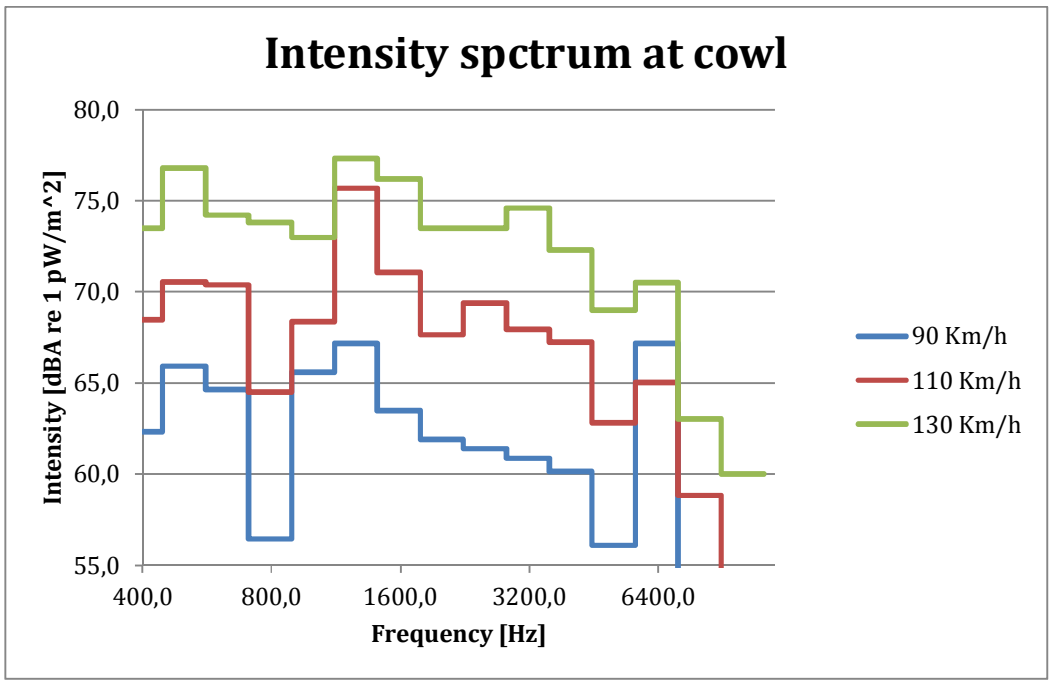

Figure 23: Sound intensity at cowl area at different wind speeds.

Compared to intensity at aforementioned points, intensity at hood and cowl area is more evenly distributed. However, two peaks and three peaks of intensity can be identified in the frequency spectrum for hood and cowl area respectively. The frequencies where the maximum intensity level happens at cowl area are 500 Hz, 1250 Hz and 6300 Hz and for the hood are 630 Hz and 3150 Hz.

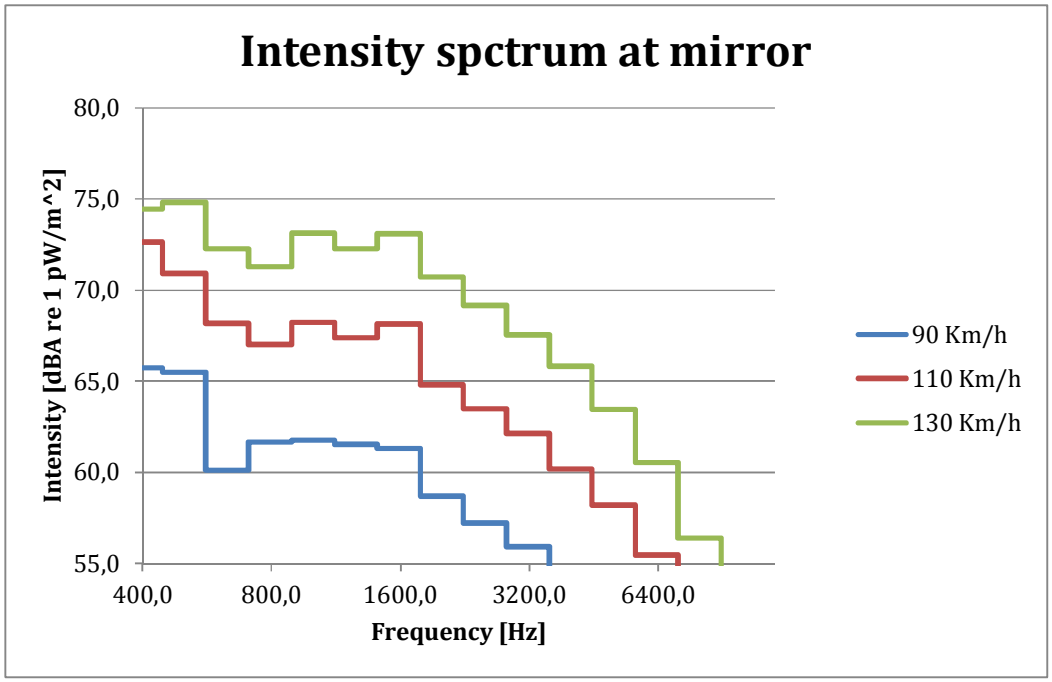

Figure 24: Sound intensity at mirror at different wind speeds.

The shape of intensity over frequency spectrum at mirror resembles that at the mirror part. In the following figure, the curves for the foot part are shifted vertically and displayed with the curves for foot since the measuring distance for the mirror part is larger than that of the foot part, which acts as a vertical shift. Once shifted, a very good similarity between intensity at foot part and that at mirror part can be observed, with exceptions only at frequency range [900 Hz ~ 1800 Hz], where peaks occur for the mirror part.

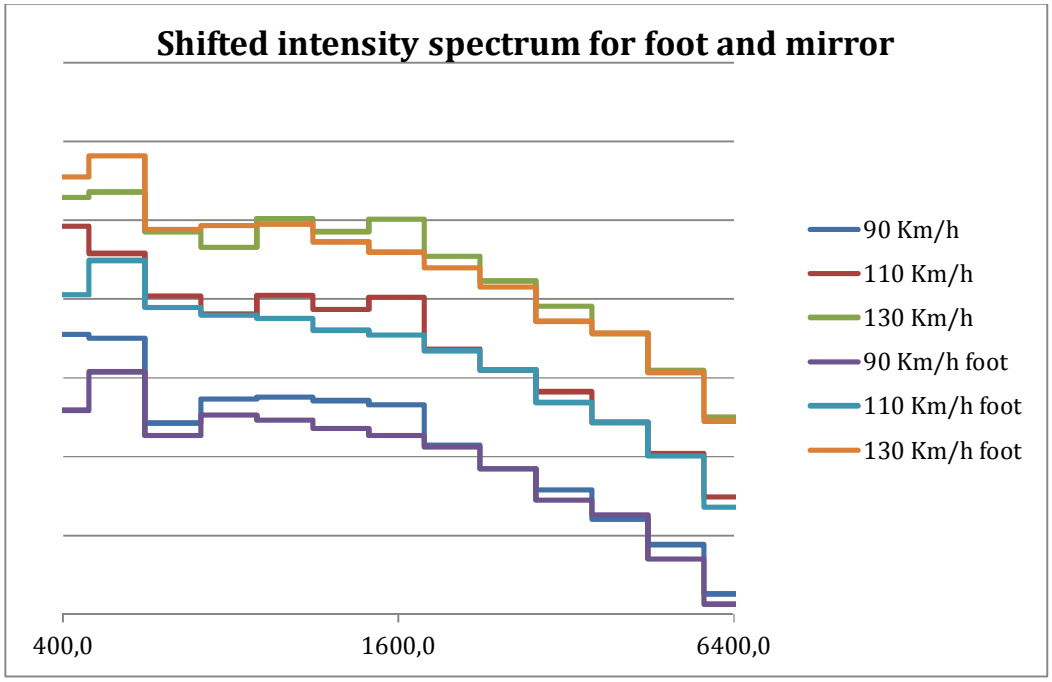

Figure 25: Sound intensity at mirror and mirror foot at different wind speeds.

One can also see that when the speed increases, the variation of intensity for a given location decreases as shown in figure below.

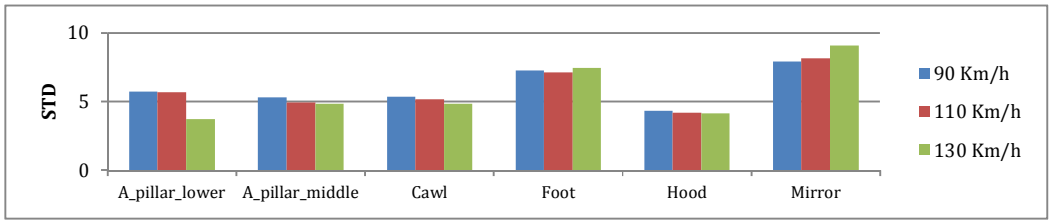

Figure 26: Sound intensity at A-pillar lower point for different wind speeds.

In Fig. 26, for four out of six locations, the STD of sound intensity is lower at 130 Km/h than the other two wind speeds. The reason is that when the speed increases, the high frequency component will be more substantial which will make the intensity curve more level, thus STD will decrease.
Result can also been seen that frequencies corresponding to peak noise are independent of wind speed, indicating that resonance is the main cause for the noise at every part measured.

4 Exterior Numerical Simulation

In this chapter, a CFD simulation of a Volvo V70 model is ran in Ansys Fluent. By investigating the vortex structure and flow around the V70 model, main wind-induced sound around the car exterior are validated. Furthermore, two improved post-processing methods are proposed.
The reason why CFD technique is used here are:
1) CFD can visualize flow and vortex around the car;
2) Surface pressure fluctuations, which are closely related to sound is easily accessible at any point over the model surface.

4.1 Simulation setup

A full-scale Volvo V70 model with total number of elements around 69 million together with a simplified Volvo wind tunnel model has been simulated in Ansys Fluent software by colleges at Volvo under three different wind speeds: 90 Km/h, 110 Km/h and 130 Km/h. The simulation method is Large Eddy Simulation (LES) and model is Smagorinsky subgridscale model. Despite large number of elements, some differences between simulation model and the real life car still exist as listed in Table 1 below.

Table 1: Difference between model and reality.

Car	Numerical model	Experimental setup
Underbody	Flat, simplified	Real
Rims	Covered rims, simplified	Real
Cowl cavity	Simplified	Real
Front grill	Closed	open
Split lines and gaps	Connected	Taped
Wheels	Fixed	Rotating

In the beginning, a stationary calculation is conducted until the convergence, then the transient simulation (RANS) is done based on the previously obtained values. When the result converges again, the simulation is done with unsteady statistics stored.
Values of RMS pressure at different parts of a Volvo V70 from CFD analysis is shown in Table 2 and Fig. 29 below.
Given the fact that the intensity probe is not measuring on a single point but rather an area with the size of 0.1 m^2 if the distance between the probe and the measuring plane is 170 mm (which is used in our case), the meshing are cut into different regions where the area weighted average of rms pressure are calculated. The function used is iso-clip in Fluent (2009).
Standard postprocessing method currently adopted by Volvo Cars is to measure pressure fluctuations over the whole wall part (with the same PID as shown in Fig. 27), which overestimates the sound source size and underestimates the average pressure fluctuation value.

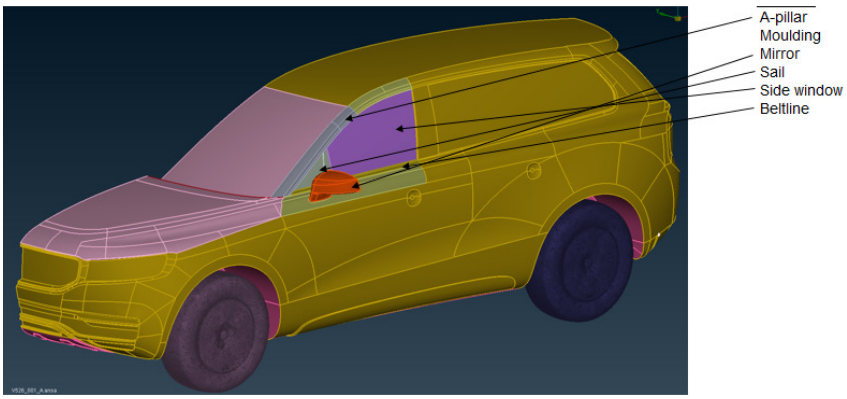

Figure 27: A Volvo V70 model with PID.

Fig. 28 shows different regions used to do the calculation. The green region represents the area measured on the front hood. Similarly, purple represents cowl cavity, red and yellow of different transparencies represent A-pillar lower, middle, upper, light blue represents rear view mirror foot, and dark blue represents rear view mirror.

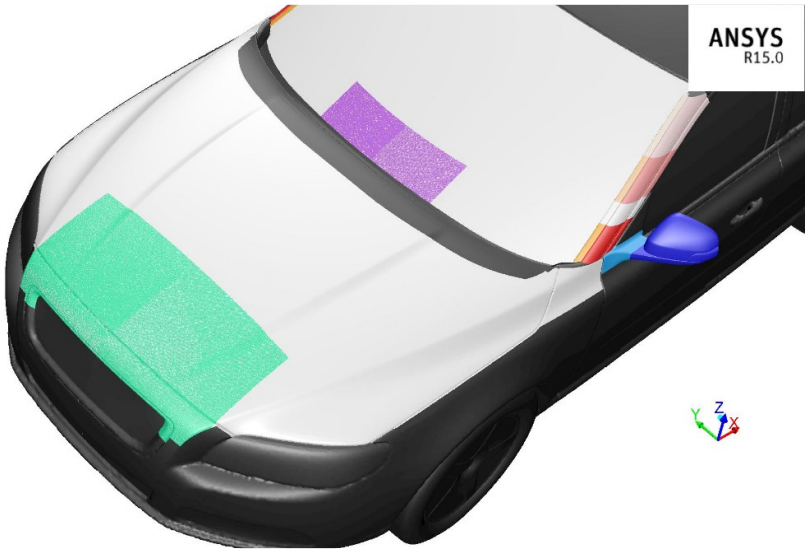

Figure 28: RMS pressure at speed of 130 Km/h.

4.2 Results

Table 2: Area weighted RMS pressure [Pa] at different locations of Volvo V70 in simulation.

Various Locations	*90* [Km/h]	*110* [Km/h]	*130* [Km/h]
A_pillar_lower	50	79	109
A_pillar_middle	31	46	65
A_pillar_upper	24	39	54

Cowl	13	18	24
Foot	35	51	72
Hood	13	21	25
Mirror	24	35	50

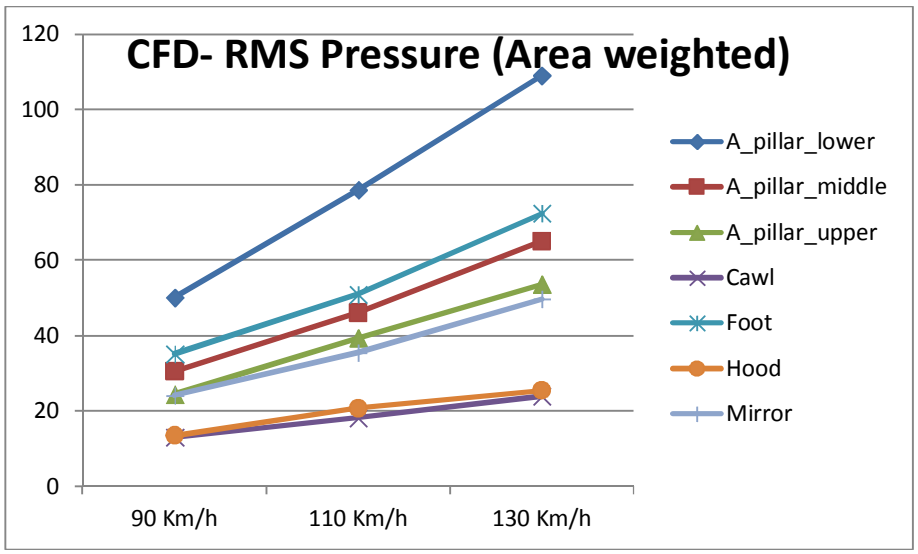

Figure 29: Area weighted rms pressure of different parts in simulation.

4.3 Analysis

From the figure above, one can conclude that A-pillar has the highest rms pressure value, followed by mirror. In addition, for all different locations listed above, the pressure RMS value increases with wind speed in a rather linear manner. Contrary to the writer's expectations, the rms pressure on rear view mirror and cowl cavity is not as high as expected. This discrepancy will be further analysed in the next section.

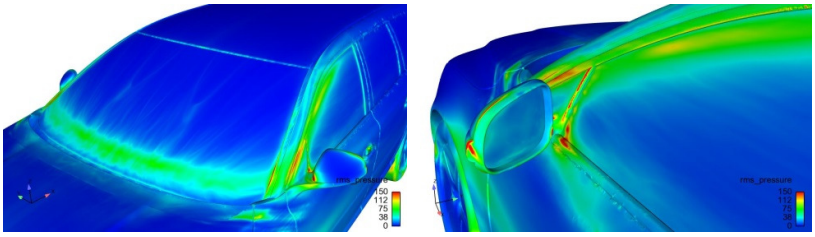

Figure 30: RMS pressure at speed of 110 Km/h.

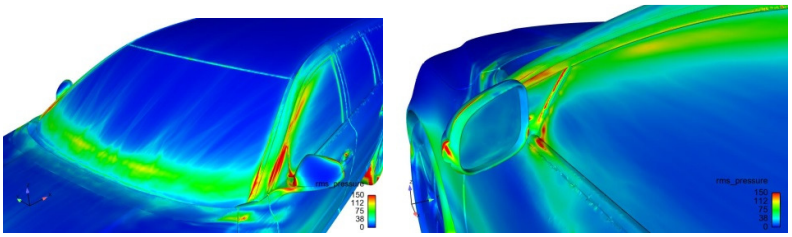

Figure 31: RMS pressure at speed of 130 Km/h.

As can be seen from the figure above, there is an observable increase in RMS pressure value when the wind speed increases.
In current process for plotting rms pressure in fluent, the upper limit is set to 150. Below is a comparison of rms pressure contours with 100 and 150 as clip value. One can clearly see that rms pressure contour with 100 clip value has a better resolution at cowl cavity area front hood and A-pillar. Thus, we recommend decreasing clip value to 100 at wind speed of 130 Km/h.

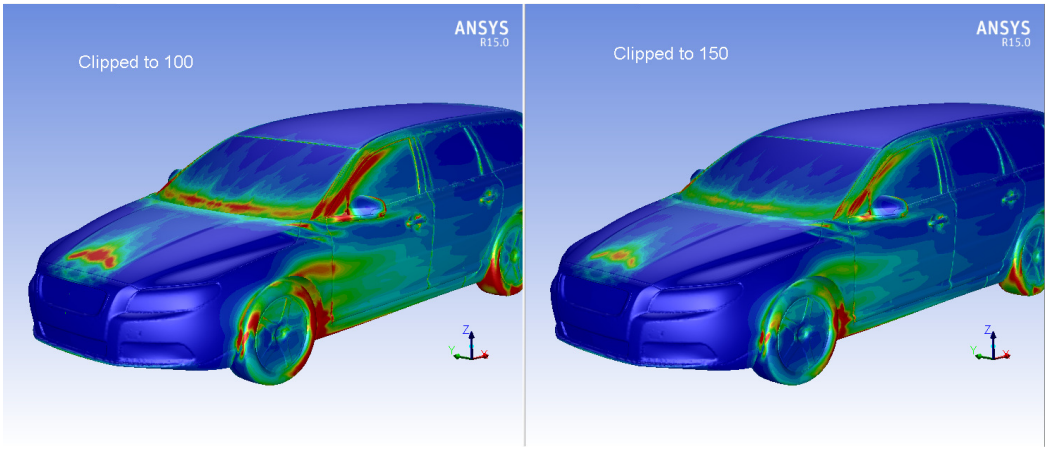

Figure 32: RMS pressure contour at 130 Km/h wind speed with clip value of 100 and 150

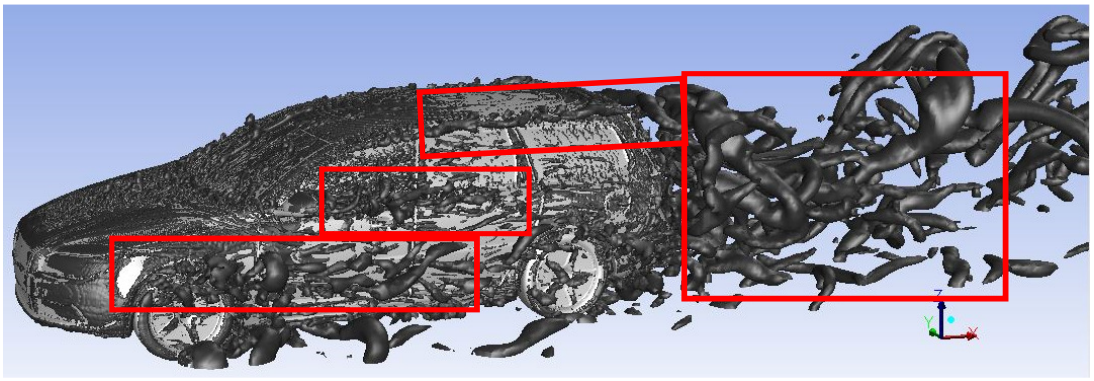

Figure 33: Vortex depiction around a Volvo V70.

Red rectangles in the figure above show the vortex generated around tire, rear view mirror, A-pillar and trunk area from front to rear accordingly. The vertex figure is generated in Fluent using Q criterion discussed by Holmén (2012) and Haller (2005) with value set to 8000. This coheres well with the reality, i.e., tire,

rear view mirror, A-pillar and trunk area are the major sources in the aerodynamic noise generation on a car.

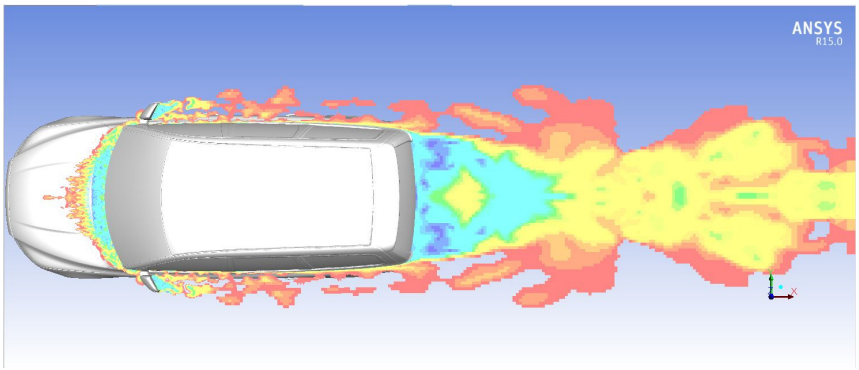

Figure 34: Vortex after rear view mirror and car trunk.

In this figure, one can also see the vortex dragging (Karman street discussed by Wille (1960) more precise) along A-pillar and trunk. Tire vortex and A-pillar vortex are not visible since the display plane of pressure contour is set to be at the same height as rear view mirror.
Still, one can see the flow separation and small vortices in the cowl and font hood area as shown in figures below, thus front hood and cowl area are also exterior noise contributors on a car.

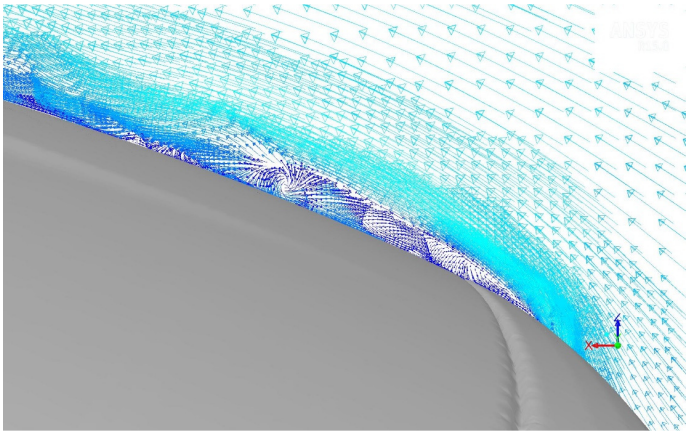

Figure 35: Vortex at front hood.

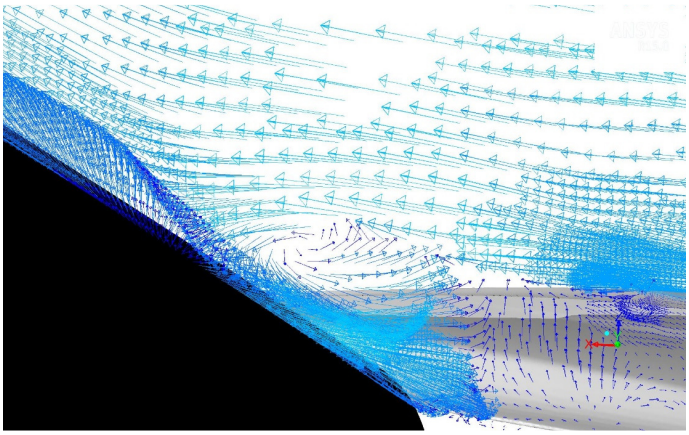

Figure 36: Vortex at cowl area.

4.4 Exterior simulation and experiment comparison

In CFD simulation, the trend that RMS pressure on A-pillar is dominant coheres with the experiment data from the intensity probe. In addition, both the intensity and the RMS pressure decreases when the measuring point moves upward on the A-pillar.

Experiment data shows that cowl area has one of the highest sound intensity values, the CFD simulation, however, shows that RMS pressure value at cowl area is around 75 Pa, which is lower than A-pillar lower point and mirror foot (value of which can be as high as 150 Pa). One possible answer will be the unauthenticity of the CAD model, which fails to capture all the details of a real car. Further examination of CAD model confirms the speculation. Fig. 37 and 38 shows cowl cavity shape for simulation model and real car respectively.

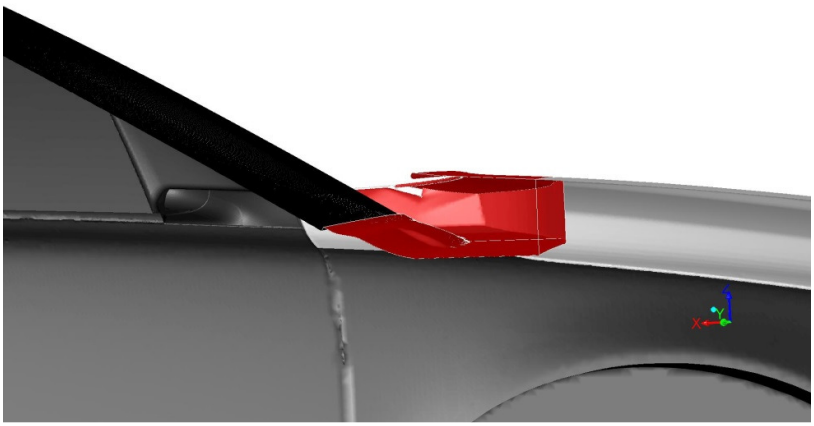

Figure 37: Cowl cavity shape for simulation model.

Figure 38: Cowl cavity shape for real car.

One can clearly see that compared to the CAD model, the shape of cowl cavity of a real V70 is narrower but longer which may have a different Eigen frequency and will induce vortices of different size and shape.

5 Interior Measurement

5.1 Introduction

5.1.1 Beamforming method

Beamforming technology can be used in noise detection to detect sound sources based on signals from sensor arrays. It has been exhaustively investigated by Van Veen and Buckley (1988), Cigada, Ripamonti and Vanali (2007). The basic principle is delay and sum method as shown in Fig. 39 below.

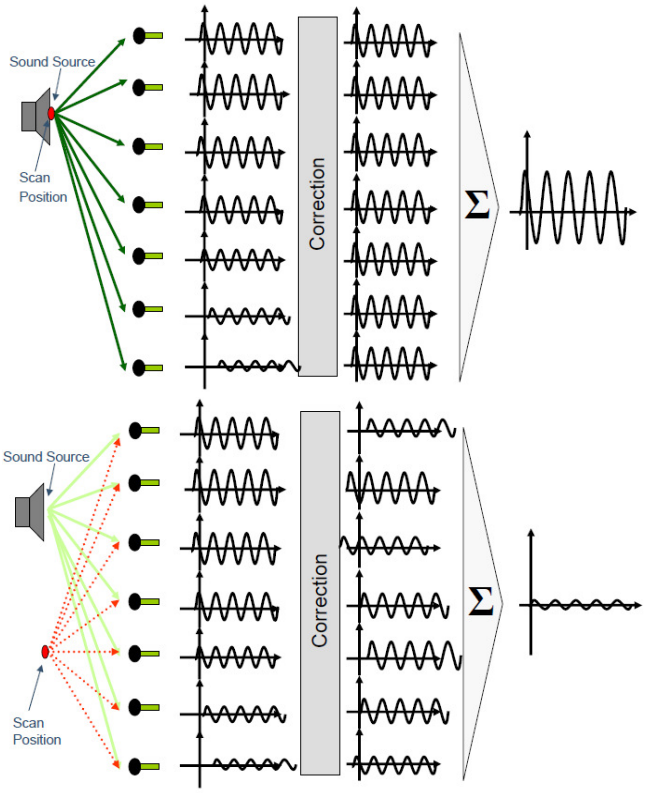

Figure 39: Beamforming: different output signals with different measurement locations.

The difference in distances from microphone to each sensor will result in differences of amplitude and phase in signal received. For each predefined sound source location, the difference in amplitude and phase of received signal can be decided. After that, the average of all the corrected signals will be calculated and is regarded as the signal on this predefined scan position.

If the predefined scan position matches the sound source, as shown in Fig. 39 upper, the corrected signals will be almost in phase with each other, which will lead to a substantial averaged signal.

If the predefined scan position is far from the sound source, then the corrected signals will cancel out each other, which will make the average insubstantial.

Thus, by defining enough number of scan positions in the measuring region, the sound source location in this region can be decided by interpolation.

The phase shift between two adjacent microphones can be calculated using equations below.

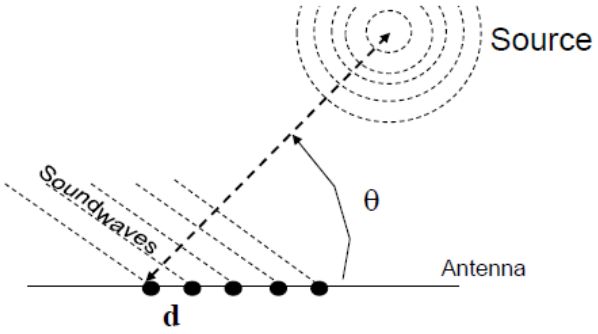

Figure 40: Beamforming theory.

$$s(t) \approx \frac{1}{N}\sum_{j=1}^{N} p_j(t-\tau_j) \tag{8}$$

$$\tau_j = \frac{dcos\theta}{c} \tag{9}$$

Where

$s(t)$ is the calculated average signal,
τ_j is the calculated time delay (phase shift),
c is the local sound speed,
θ is the angle between the sound wave and microphones plane,
d is the spacing between two adjacent microphones.

The amplitude of signal can be corrected by the equation below:

$$s_i(t) = l * s_i(t) \tag{10}$$

Where

$s_i(t)$ is the signal from i^{th} microphone,
l is the distance from microphone array to the measured location.

5.1.2 Equivalent source method

Unlike beamforming, Equivalent source method (ESM) does not calculate the exact value of source quantity. Instead, it tries to simulate the source information by replacing all the sources with monopoles under precondition that all the sources can be represented by limited number of monopoles. When the measured source distribution matches simulated ones, the source distribution can be decided. Fig. 41 shows the geometry of the equivalent source surface E and measured surface M. As studied by Kropp and Svensson (1995), the measured pressure for the m^{th} measurement point at time t can be expressed as,

$$p_m(t) = \sum_{k=1}^{K}[q_k(t) * g(R_{mk}, t)], \tag{11}$$

Where

$p_m(t)$ is the pressure at m^{th} measurement point,
$q_k(t)$ is the k^{th} equivalent source strength at time t,
R_{mk} is the distance between the k^{th} equivalent source, l^{th} measurement point,
$g(R_{mk}, t)$ is the impulsive response function between k^{th} equivalent source and m^{th} measurement point,
$*$ is the convolution sign,

K is the total number of equivalent sources.

$g(R_{mk}, t)$ is given by

$$g(R_{mk}, t) = \frac{\delta\left(t - \frac{R_{lk}}{c}\right)}{R_{mk}}, \tag{12}$$

where

$\delta(t)$ is the Dirac Delta function,
c is the sound speed.

Plug equation 12 into equation 11, yields,

$$p_m(t) = \sum_{k=1}^{K} \frac{q_k(\tau_{mk})}{R_{mk}}, \tag{13}$$

where retarded time τ_{mk} is expressed as

$$\tau_{mk} = t - \frac{R_{mk}}{c}. \tag{14}$$

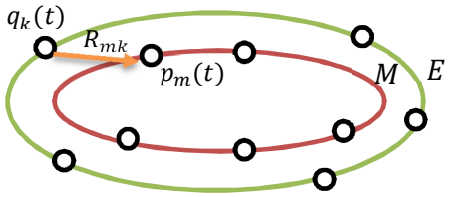

Figure 41: ESM theory.

When $p_m(t)$ is known, $q_k(\tau_{mk})$ can be solved by equation 13. Usually, the group of equations are overdetermined, thus certain algorithms are needed to get the approximated result as discussed by Bi, Geng and Zhang (2013), Gounot and Musafir (2011).

Compared to Beamforming method, a prior knowledge of measurement points is needed and the total number and location of equivalent sources must be decided. The accuracy of the simulation is heavily dependent on parameters mentioned above. Lee, Brentner and Morris (2011) have investigated sensitivity of the method to different parameters mentioned above. It was found that for low frequency source mapping, there should be 5 to 10 measurement points in a distance equivalent to the wavelength of interest and equivalent source number should be a quarter or half of the measurement point number. In addition, the position of equivalent sources should be 80% to 90% replica of the sound source surface (in the case, car interior surface) and there should be 10 points per time step. It has also been pointed out that the combinations of the parameters vary significantly on measurement frequency and sound source surface.

Compared to Beamforming method, ESM has better resolution at low frequency region and since an iteration phase is involved, only approximated value can be obtained. Moreover, for the same reason, it is more time consuming than Beamforming.

5.2 Experiment setup

5.2.1 Geometry scanning

Before measuring the sound inside the car using 3D camera, the geometry of the car needs to be scanned first. A camera and an infrared sensor are utilized as shown in Fig. 42.

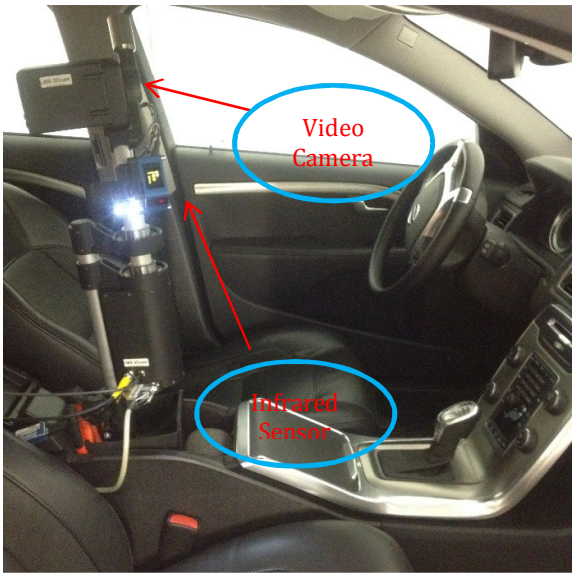

Figure 42: Geometry scanning device.

The video camera is used to capture the interior of the car and the infrared sensor is used to detect the distance from the measuring device to the car interior. The transparent part of car exterior is covered by an opaque sheet of cloth to ensure accurate reading of infrared sensor as shown in Fig. 43. After the scanning, a similar picture like Fig. 44 below can be generated. The rendering of car interior might be slightly different with different meshing sizes. The meshing size selected in this project is 3000.

Figure 43: A Volvo V70 during scanning.

Figure 44: Scanned geometry of a Volvo V70.

5.2.2 Sound measurement

A spherical 3D acoustic camera consists 36 microphones is used in the measurement process. Details are listed below:

- Frequency range 200 Hz to 8 kHz
- Diameter 30 cm, 36 microphones of G.R.A.S. Type 40PH
- One mono-connector with 36 channels
- 2 MP auto-focus camera
- Tripod and mounting frame for in the cavity

As mentioned before, one disadvantage of the acoustic camera used in our experiment is the low dynamic range that means some weaker sources could possibly be masked by other stronger sources. In addition, according to prior knowledge, rear car body can generate large amount of noise, thus, for masking prevention, front and rear of car are separated using heavy layer as shown in figure below. A heavy layer consists of a stiff rubber layer and thick foam layer that sticks to it and it is used to damp out noise from the rear.

Figure 45: Spherical camera in a car.

Figure 46: A heavy layer in the car.

Moreover, for some configurations, B-pillar and two rear doors are also sealed to prevent influence of leakage as shown in figure below.

Figure 47: A heavy layer on side window.

In order to see how one specific exterior component affects interior compartment sound level, a cord is put on rear view mirror and A-post as an extra feature to simulate sharp edges as shown in Fig. 48 and Fig. 49 below.

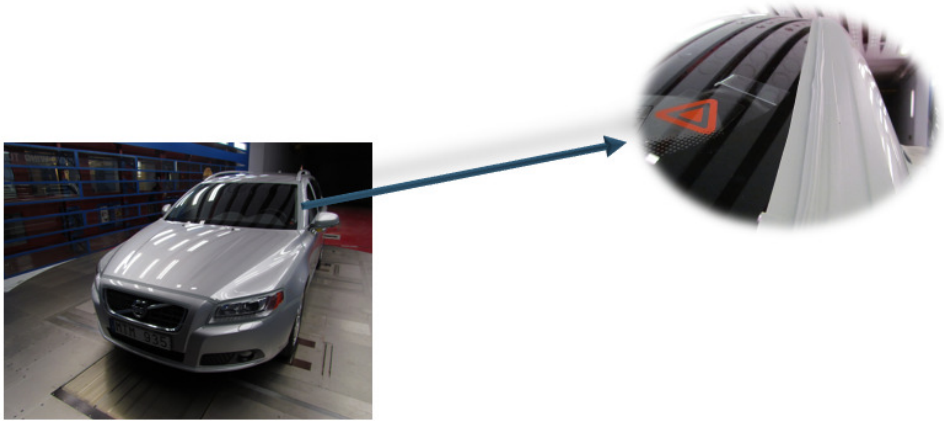

Figure 48: A cord as an extra feature on the A-post.

Figure 49: A cord as an extra feature on rear view mirror.

Because of its lightweight and slimness, a G.R.A.S 40LS ¼" surface microphone is deployed and put on different locations at car exterior surface as shown in Fig. 50. Signal gathered by it will be sent to the front end and serves as reference signal for coherence analysis.

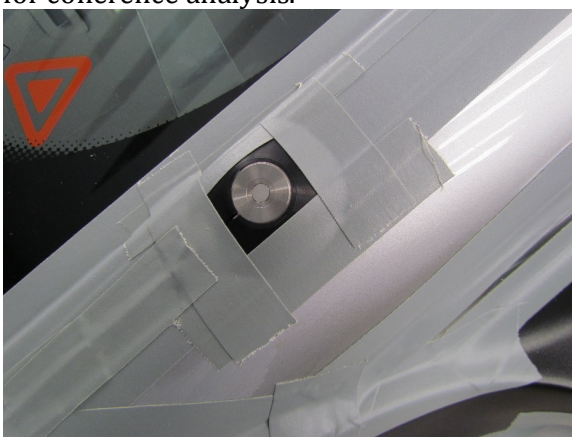

Figure 50: A surface microphone on the A-post.

The surface microphone is taped in a way that minimum interference is exerted. A detailed table containing all the configurations done in the experiment can be found in Appendix B.

Method and study object selection

Figures below show a comparison between interior sound with and without heavy layer. One can see that trunk area is the largest sound source inside the car at frequencies from 180 to 1500 Hz. Still, heavy layer decreases the noise level from the rear by 4 dB.

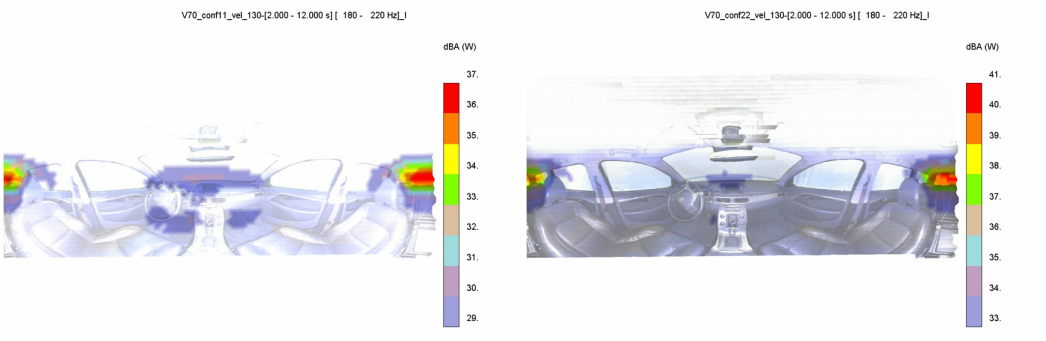

Figure 51: Left: With heavy layer. Right: Without heavy layer.

It was found out (as is also stated in the user manual) that during post processing process quantification (based on Equivalence Source Method) has turned out to

be a better map averaging method than localization (based on near field beamforming) since it enables a better resolution at low frequencies. Figure below shows a comparison of sound mapping at low frequency range using two methods mentioned above. The frequency range is [1130Hz 1410Hz] and the calculation time range is [0s 15.195s].

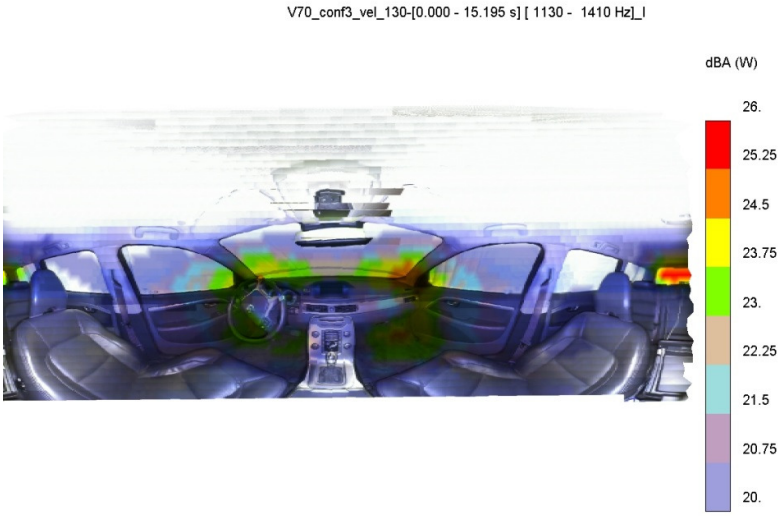

Figure 52: Source mapping using Equivalent Source Method at frequency [1130Hz 1410Hz]

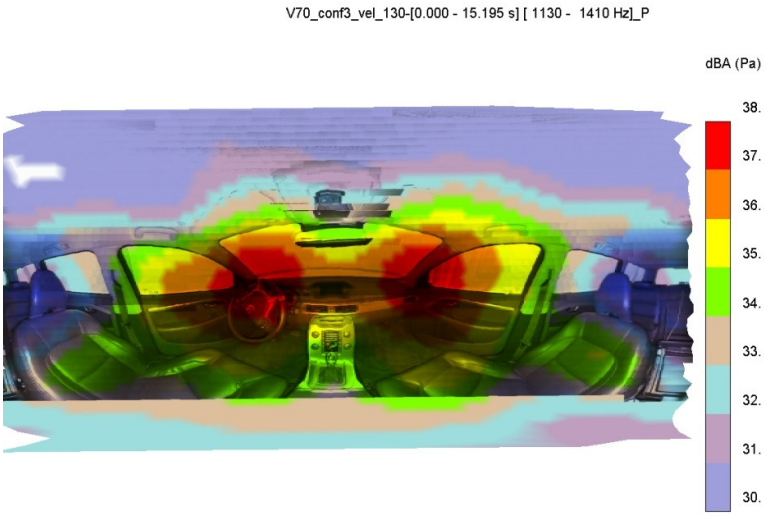

Figure 53: Source mapping using near field beamforming method at frequency [1130Hz 1410Hz]

Figure below shows a comparison of sound mapping at low frequency range using two methods mentioned above. The frequency range is [3570Hz 4480Hz] and the calculation time range is [0s 15.160s].

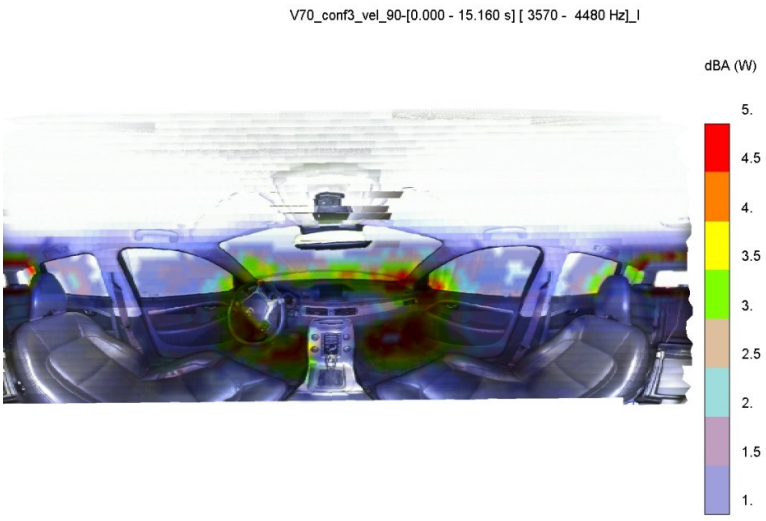

Figure 54: Source mapping using Equivalent Source Method at frequency [3570Hz 4480Hz]

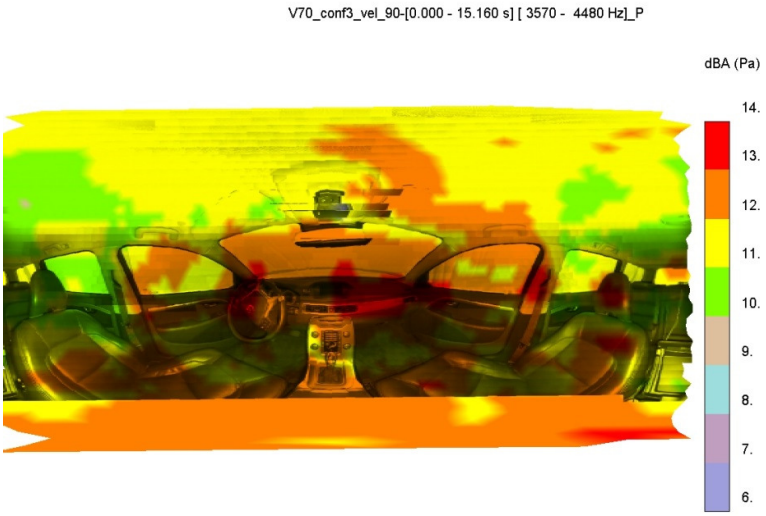

Figure 55: Source mapping using near field beamforming method at frequency [3570Hz 4480Hz]

As can be seen from figures above, area of sound source on the mapping using ESM is smaller than that obtained using near field beamforming method in both low and high frequency ranges. In Fig. 54, one can see mainly it is two A-pillar are radiating power in the front, while in Fig. 55, hardly can one reach the same conclusion since the area that radiates power is too big to tell whether the source is A-pillar or side window glass.

However, one drawback of quantification method is that it is time consuming. For the map averaging using localization/principal component method for a segment of signal [4s 7s] [3570Hz 4480Hz], the elapsed time is 27s; while the elapsed time of the same segment using quantification method has reached 1000s. Thus, it is impractical to postprocess every case using quantification method.

In this thesis work, the following approach is used: every case is processed using localization method in the low frequency range [180Hz 560Hz], and quantification method is used in the high frequency range [570Hz 5650Hz].
Still, radiation patterns of conf. 13 and conf. 14 at 90 Km/h wind speed and that of conf. 3 and conf. 4 at 130 Km/h wind speed are compared, near identical radiation patterns can be observed for configurations between which the only difference being outside pressure sensor locations, one example being Fig. 56 and 57 below. Thus, one may conclude that outside pressure sensor location has an ignorable impact on the interior noise radiation pattern.

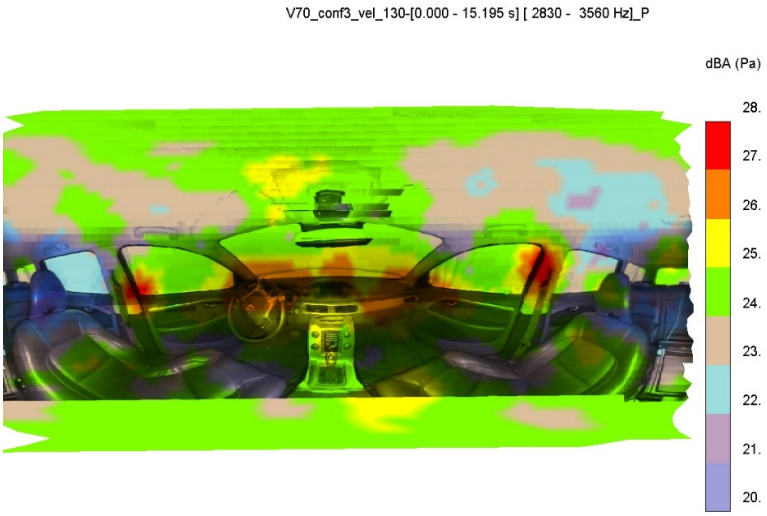

Figure 56: Interior noise radiation pattern for conf. 3 at [0s 15s], [2830Hz 3560 Hz]

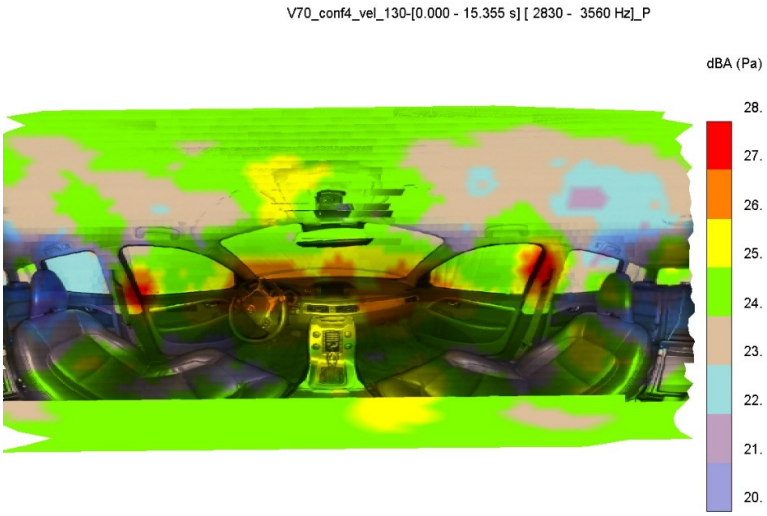

Figure 57: Interior noise radiation pattern for conf. 4 at [0s 15s], [2830Hz 3560 Hz]

Moreover, a comparison of noise radiation patterns for one configuration at different wind speeds reveals that variation of wind speed will not influence the interior noise radiation pattern (but only the overall level of noise) as shown in Fig. 58, 59 and 60.

Figure 58: Interior noise radiation pattern for conf. 3 at [0s 15s], [1790Hz 2240 Hz] at wind speed 90 Km/h.

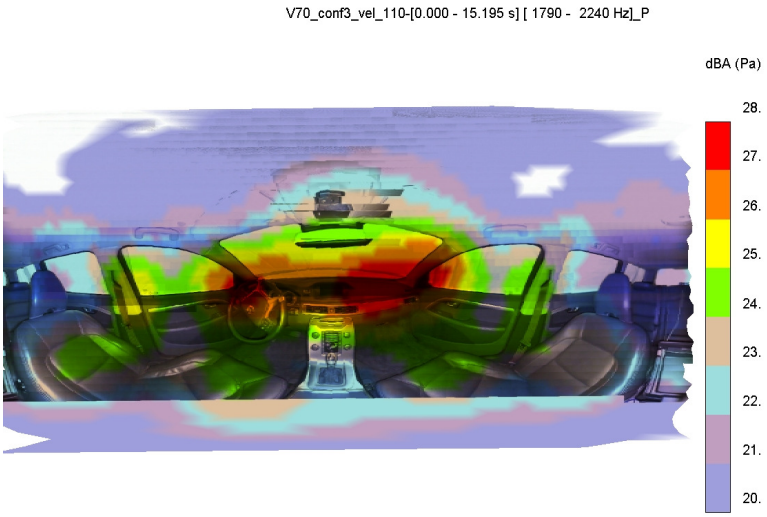

Figure 59: Interior noise radiation pattern for conf. 3 at [0s 15s], [1790Hz 2240 Hz] at wind speed 110 Km/h.

Figure 60: Interior noise radiation pattern for conf. 3 at [0s 15s], [1790Hz 2240 Hz] at wind speed 130 Km/h.

Thus, for the analysis of interior noise radiation patterns, conf. 3 at 130 Km/h wind speed is selected.

5.3 Result and analysis

5.3.1 Coherence analysis

A coherence analysis proposed by Bendat and Piersol (1980) is achieved using signal gathered by exterior microphone and all the 36 interior microphones. The coherence is calculated in software LMS Test.Lab. Fig. 61 below is an example of coherence of exterior signal and one channel interior signal.

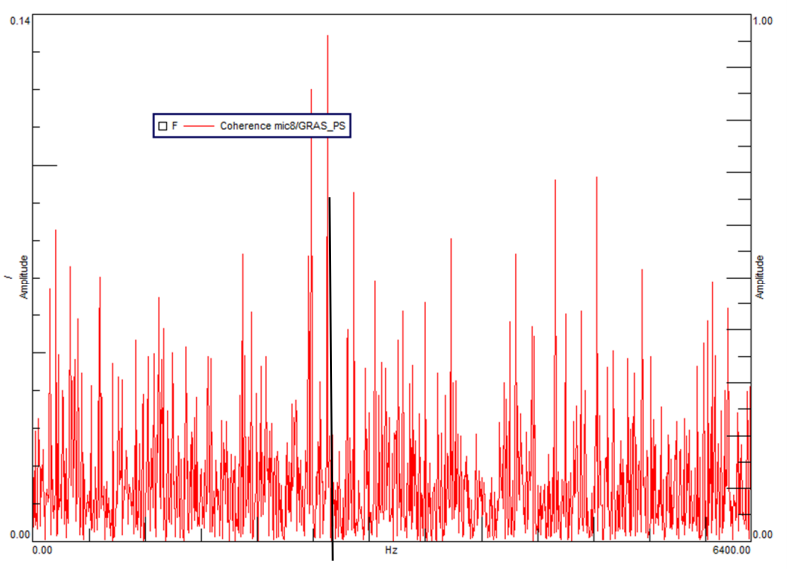

Figure 61: Coherence for exterior microphone and one interior microphone.

Coherence data for conf. 1, 2, 3 and 4 are then exported into *.mat format and post processed in Matlab (See Appendix C for detailed code).
As can be observed in Matlab, for the same exterior signal, the maximum coherence of this signal to each interior signal occurs almost at the same frequency (more than 80% usually). Still, a large variation of maximum coherence from each interior microphone to the exterior cannot be observed. After analysing all 12 sets of data and averaging over different wind speed for each exterior sensor location, Fig. 62 can be obtained.

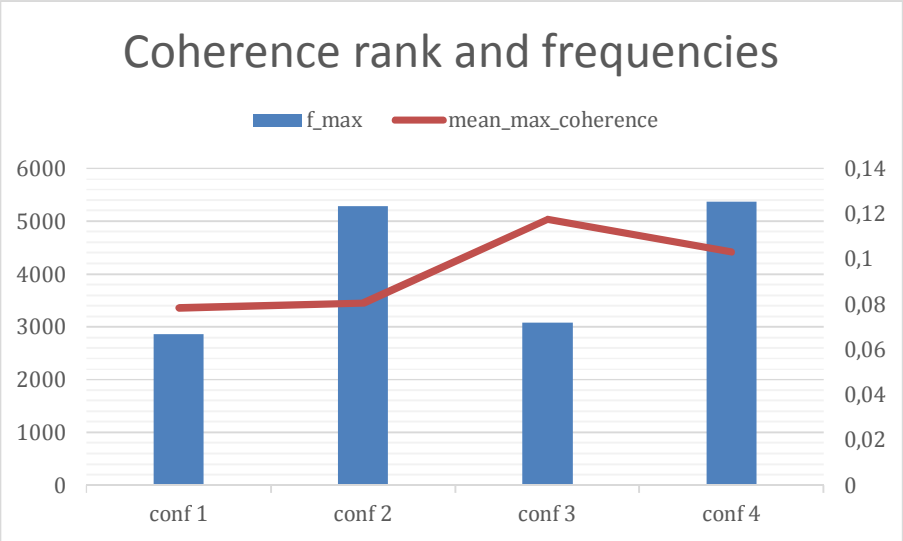

Figure 62: Coherence rank and frequencies.

One may conclude that, for the above four configurations, configuration 3 has the highest maximum coherence value, followed by configuration 4, 2 and 1. That means noise at configuration 3 (A-pillar lower point) has the largest influence on the interior noise among the four, followed by conf. 4 (side window), conf. 2 (windshield middle position) and conf. 1 (windshield low position). In addition, windshield middle and side window generated noise is dominant in the high frequency range whereas those generated by windscreen low position and A-pillar lower are dominant in the low frequency range.
However, given the overall low maximum coherence values, the conclusions made above are still dubious since the exterior reference microphone is measuring the pressure fluctuations on the car surface, which corresponds to the vibration of the car as well as air turbulence around measuring region while the interior are measuring the pressure fluctuations in the air. The interior noise can be transmitted from outside either through structure or air. The other cause for the interior noise is the resonance of some hollow parts, e.g. seat belt opening on the B-pillar, with the car mainframe. Hence, it is safe to conclude that the contribution to the total noise level in the car of transmission through structure is low. This is understandable since already many treatments have been done on the car frame on structure borne noise prevention. Thus, we may conclude that aerodynamic

5.3.2 Interior analysis

In low frequency range (180Hz to 280Hz), panel (vibration at cowl cavity) and foot area (vibration at wheel house) are dominating. As the frequency increases

(290Hz to 560Hz), only the foot area is dominating. At the frequency range (570Hz to 1120Hz), the sound is distributed quite evenly at the side window and door. This is speculated to be booming noise from structure vibration due to side window flushing. Starting from middle frequency (1130 Hz to 4480 Hz), sound at the A-post part is dominating. In addition, at high frequencies (2250 Hz to 4480 Hz), B-post parts and cowl area emerge to be one of the major contributing parts also. This is because of the opening on the B-post of which the seat belt comes out. Fig. 63, 64 and 65 below show the typical radiation pattern at three different frequency ranges.

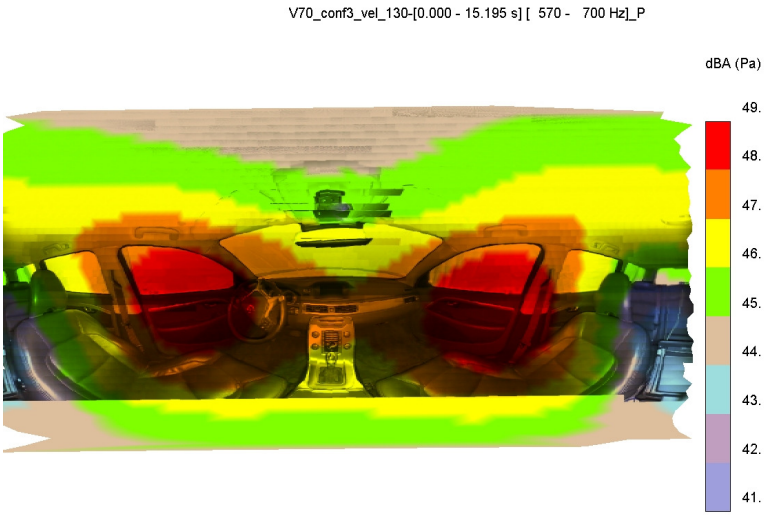

Figure 63: Interior noise radiation pattern for conf. 3 at [0s 15s], [570 - 700 Hz] at wind speed 130 Km/h.

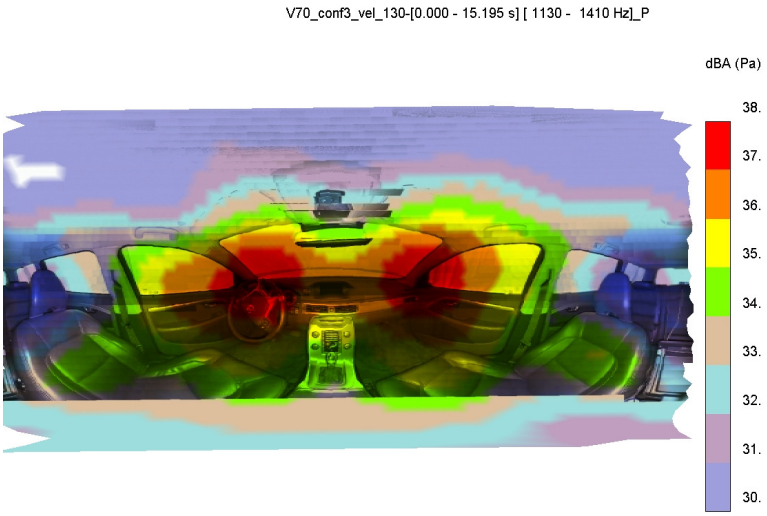

Figure 64: Interior noise radiation pattern for conf. 3 at [0s 15s], [1130 - 1410 Hz] at wind speed 130 Km/h.

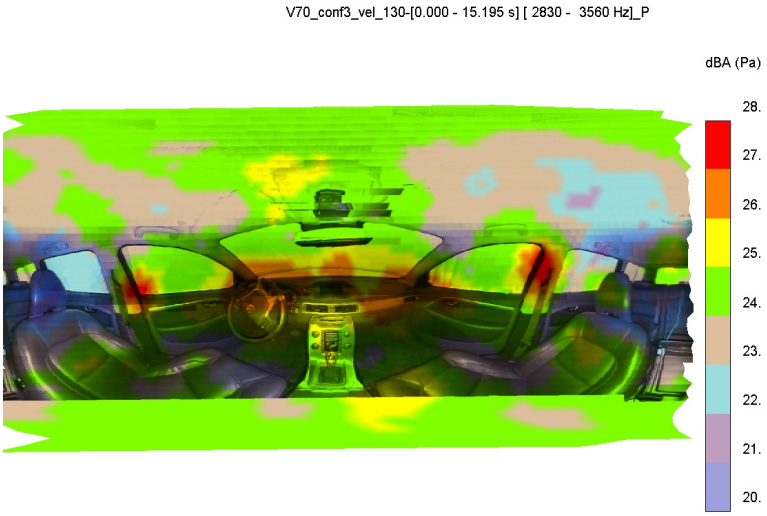

Figure 65: Interior noise radiation pattern for conf. 3 at [0s 15s], [2830 - 3560 Hz] at wind speed 130 Km/h.

Figures below are radiation patterns for conf4 and conf5 respectively with only difference being position of the right rear view mirror.

Figure 66: Interior noise radiation pattern for conf. 4 at [2s 12s], [570 - 700 Hz] at wind speed 130 Km/h.

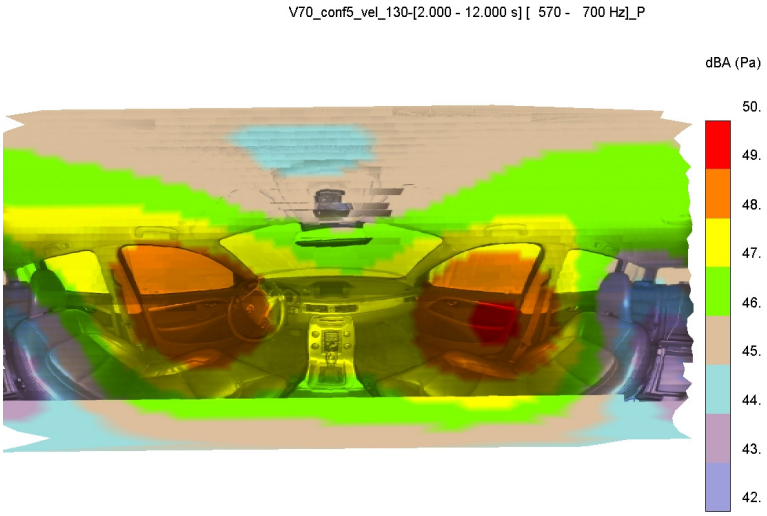

Figure 67: Interior noise radiation pattern for conf. 5 at [2s 12s], [570 - 700 Hz] at wind speed 130 Km/h.

From Fig. 66 and 67 it can be concluded that at the frequency range (570Hz to 1120Hz), the booming noise is the flushing noise generated from rear view mirror vortex.
Table below shows the radiation pattern over different frequencies.

Table 3: Influence of different exterior part on interior compartment noise.

	[180 - 280 Hz]	[290 - 560 Hz]	[570 - 1120 Hz]	[1130 - 1410 Hz]	[2250 - 5650 Hz]
Dashboard					
Foot rest					
Side window & Front side door					
A-post					
B-post					
Cowl					

5.3.3 Relating to the outside sound

By comparing radiation pattern of different configurations, effects of different exterior component i.e., BLIS (conf. 11 and conf. 12), A-post (conf. 14 and conf. 15), mirror (conf. 14 and conf. 16) and openings in the compartment (conf. 14 and conf. 19) on the interior sound level can be determined (see figures below).

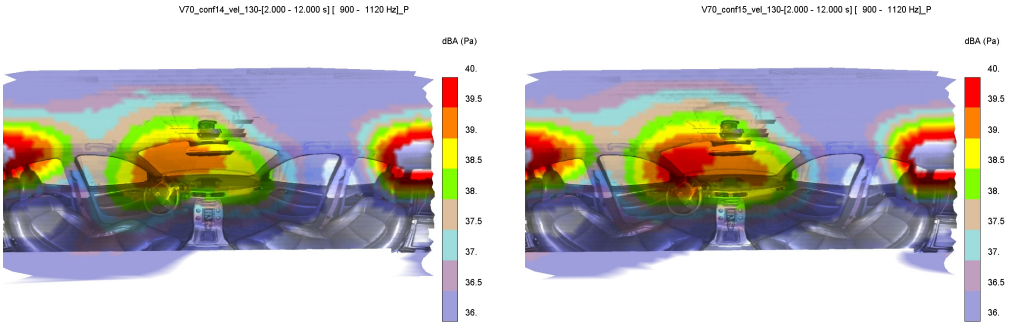

Figure 68: Compartment sound distribution at Frequency [900 - 1120] Hz

, Left: Without A-post cord Right: With A-post cord

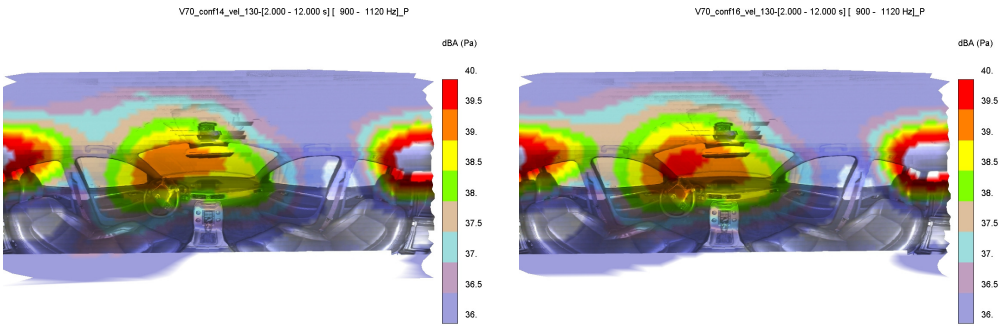

Figure 69: Compartment sound distribution at Frequency [710 - 890] Hz

Left: Without rear view mirror cord Right: With rear view mirror cord

One can see that existence of cord has an overall negative influence on the compartment sound level. It can also be observed that for some of the frequency bands, cord improved the sound level inside the compartment. This can be explained by the fact that Volvo wind tunnel is not an acoustic wind tunnel; previous benchmark test shows that noise brought by wind tunnel itself is substantial in low frequencies.

Table 4: Area weighted rms pressure of different parts in simulation.

	[180 - 220 Hz]	[230 - 280 Hz]	[290 - 350 Hz]	[360 - 440 Hz]	[450 - 560 Hz]	[570 - 700 Hz]	[710 - 890 Hz]	
BLIS	-	+		-	-	-	-	
A-post		+	+		-			
Mirror	-		+			-	++	
Dashboard and door vavities	-	-			+	-	-	
	[900 - 1120 Hz]	[1130 - 1410 Hz]	[1420 - 1780 Hz]	[1790 - 2240 Hz]	[2250 - 2820 Hz]	[2830 - 3560 Hz]	[3570 - 5650 Hz]	
BLIS	-			-				
A-post	--		-	-	-	-		
Mirror	-	+	-			-		
Dashboard and door vavities	-	-	-	-	-	-	-	
Notes:	-	means the presence of change (the cord) makes the sound level in the compartment worse in the given frequency range						
	+	means the oppsite						
		means no big difference observed						

6 Conclusions and Future Work

6.1 Conclusions

In this work, wind-induced sound inside and outside a Volvo V70 has been investigated. Following are the conclusions of the thesis project, which correspond to the scope of work part, Chapter 1.

1. Exterior sound sources measured with probe
   a) Foot and cowl area are dominant sound sources measured with intensity probe in the flow field
   b) Foot with BLIS dominates at low frequencies (till 1100 Hz) (probe)
   c) Cowl dominates at high frequency (probe)
   d) Intensity at hood and cowl are more evenly distributed
2. CFD simulation
   a) Low pressure fluctuations at cowl in CFD simulation is due to simplified structure of CFD model
3. 3D Camera
   a) ESM is a better method than Beamforming, especially at low frequencies
   b) But it's more time consuming
   c) No coherence has been found between outside surface pressure fluctuations and inside SPL
4. The influence of exterior wind-induced noise on the compartment sound level can be described by Table 3.

6.2 Summary of contributions

This thesis offers the following contributions:

- Proposing a way to compare and rank exterior sound source using intensity probe;
- Improving two postprocessing methods for CAE currently used by Volvo Cars Corporation;
- Conducting a study on the sound distribution inside a compartment;
- Pinpointing the influence of each exterior component to the sound distribution inside compartment at each frequency band;
- Through coherence analysis, it has been decided that wind-induced sound is not directly related to component structural vibration but to flow separation and vortex breaking.

6.3 Future research

Given the limited time, some of the work has not been fully implemented. In addition, failure encountered at the experiment process has shed more light on the project. Therefore, to understand related issue better, following are recommended to be implemented in future time.

1. More emphasis on the rear of the car for study of aerodynamic noise;
2. Transfer path analysis for wind generated noise;
3. Include wheels rotation;
4. Test with 3D CAM in aeroacoustical wind tunnel;
5. Perform road test.

7 References

Jacobsen (1991): A simple and effective correction for phase mis-match in intensity probes. *Applied Acoustics*, Vol. 33, No. 3, 1991, 165-180.

Chung and Blaser (1981). Recent developments in the measurement of acoustic intensity using the cross-spectral method, SAE Technical Paper.

Jacobsen and De Bree (2005): Measurement of sound intensity: pu probes versus pp probes. *Proceedings of NOVEM*, Vol. No. 2005.

Thompson and Tree (1981): Finite difference approximation errors in acoustic intensity measurements. *Journal of Sound and Vibration*, Vol. 75, No. 2, 1981, 229-238.

Fahy (2002): *Sound intensity*. CRC Press, 2002.

Jacobsen (2003): Sound intensity and its measurement and applications. *Current Topics in Acoustical Research*, Vol. 3, No. 2003, 87-91.

Jacobsen (1993): Sound intensity measurement at low levels. *Journal of sound and vibration*, Vol. 166, No. 2, 1993, 195-207.

Jacobsen, Cutanda and Juhl (1998): A numerical and experimental investigation of the performance of sound intensity probes at high frequencies. *The Journal of the Acoustical Society of America*, Vol. 103, No. 2, 1998, 953-961.

Kinsler, Frey, Coppens and Sanders (1999): Fundamentals of acoustics. *Fundamentals of Acoustics, 4th Edition, by Lawrence E. Kinsler, Austin R. Frey, Alan B. Coppens, James V. Sanders, pp. 560. ISBN 0-471-84789-5. Wiley-VCH, December 1999.*, Vol. 1, No. 1999.

Fluent (2009): 12.0 Documentation. *Ansys Inc*, Vol. No. 2009.

Holmén (2012): Methods for Vortex Identification. *Master's Theses in Mathematical Sciences*, Vol. No. 2012.

Haller (2005): An objective definition of a vortex. *Journal of Fluid Mechanics*, Vol. 525, No. 2005, 1-26.

Wille (1960): Karman vortex streets. *Advances in Applied Mechanics*, Vol. 6, No. 1960, 273-287.

Van Veen and Buckley (1988): Beamforming: A versatile approach to spatial filtering. *IEEE assp magazine*, Vol. 5, No. 2, 1988, 4-24.

Cigada, Ripamonti and Vanali (2007): The delay & sum algorithm applied to microphone array measurements: numerical analysis and experimental validation. *Mechanical systems and signal processing*, Vol. 21, No. 6, 2007, 2645-2664.

Kropp and Svensson (1995): Time-domain formulation of the method of equivalent sources. *Acta Acustica*, Vol. 3, No. 1, 1995, 67-73.

Bi, Geng and Zhang (2013): Cubic spline interpolation-based time-domain equivalent source method for modeling transient acoustic radiation. *Journal of Sound and Vibration*, Vol. 332, No. 22, 2013, 5939-5952.

Gounot and Musafir (2011): Simulation of scattered fields: some guidelines for the equivalent source method. *Journal of Sound and Vibration*, Vol. 330, No. 15, 2011, 3698-3709.

Lee, Brentner and Morris (2011): Assessment of time-domain equivalent source method for acoustic scattering. *AIAA journal*, Vol. 49, No. 9, 2011, 1897-1906.

Bendat and Piersol (1980): Engineering applications of correlation and spectral analysis. *New York, Wiley-Interscience, 1980. 315 p.*, Vol. 1, No. 1980.

Appendix A

One of the difficulties encountered is that a warning will pop up when one tries to open a measurement file in LMS Test.Lab 3D Acoustic Camera Advanced software without any connections to the hardware, stating that IR channels are defined without connection with any IR sensors. As shown in fig below, in this condition, the next button cropped out in red rectangle is grey. According to the error message, this can be solved by loading 3DCam.tpl before loading any other files.

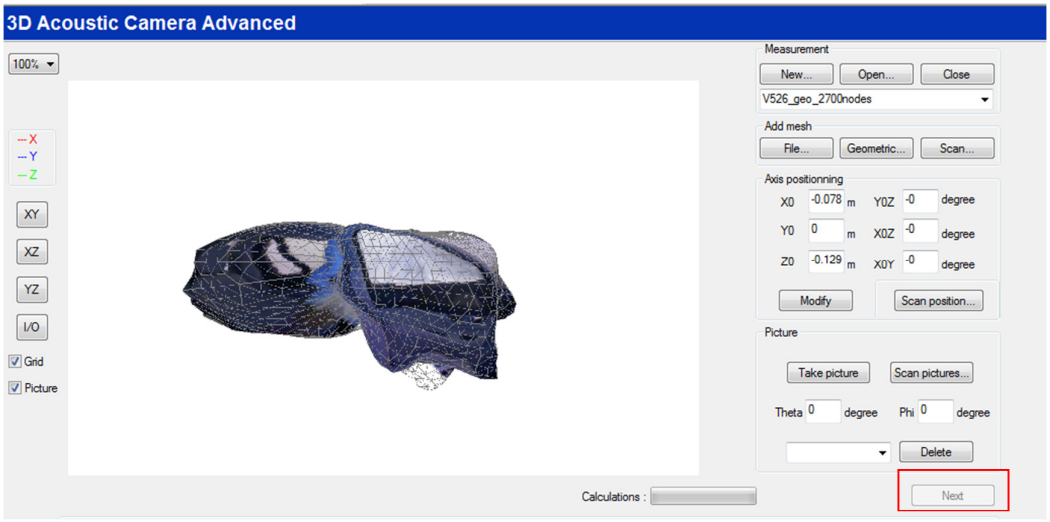

Appendix B

Below are the details for different configurations.

	All configurations are ran at 90, 110 and 130 km/h.					
	Heavy layer behind the front seats	absorption panels on the left walls	rear side windows covered by absorption	PS location	mirror location	front and front doors are taped
Conf 1	x	x	x	windscreen low postion in the middle near cawl cavity		x
Conf 2	x	x	x	Windscreen middle position		x
Conf 3	x	x	x	A post lower point		x
Conf 4	x	x	x	Side window		x
Conf 5	x	x	x	side window	RHS mirror as LHS	x
Conf 6	x	x	NO	side window	RHS mirror as LHS	x
Conf 7	x	x	NO	NO, but ps channel not disabled	RHS mirror as LHS	x
Conf 8	NO	x	NO	NO, but ps channel not disabled	RHS mirror as LHS	x
Conf 9	NO	x	NO	NO, but ps channel not disabled		NO
Conf 10	NO	NO	NO	NO, but ps channel not disabled		NO

Continue Week 17.		Heavy layer on the rear (in the trank)	rear side windows covered by absorption	extra carpits on the floor	mirror location standart for LHS and RHS	front and doors are taped	RHS front door in covered	LHS mirror modeled by yellow clay	LoudSpeaker on the door with form and air inlet on the dash board taped						
	Conf11	X	X	X	X	X	X	X	X						
	Conf12	X	X	X	X	X	X	X	X						
	Conf13	X	X	X	X	X	X	X		LHS crashes and we rerun with new project name					
	Conf14	X	X	X	X	X	X	X	X		BUS ON BUS OFF	**NEW REF!!!**			
	Conf15	X	X	X	X	X	X		X		BUS OFF	A-post cord (as extra feature)			
	Conf16	X	X	X	X	X	X		X		BUS OFF	A-post cord (as extra feature) Removed	Corde on reare view mirror		
	Conf17	X	X	X	X	X	X		X		BUS OFF	A-post cord (as extra feature) Removed	Corde on reare view mirror	extra tape on air inlet and small speaker,	
	Conf18	X	X	X	X	X	X		X		BUS OFF	A-post cord (as extra feature) Removed	Corde on reare view mirror	extra tape on air inlet and small speaker, defroster and door stop on the RHS	the RHS absorption material on the front removed
	Conf19	X	X	X	X	X	X		X		BUS OFF	A-post cord (as extra feature) Removed		extra tape on air inlet and small speaker, defroster and door stop on the RHS	the RHS absorption material on the front removed
	Conf20	X	X	X	X	X	X		X		BUS OFF	A-post cord (as extra feature) Removed		extra tape on air inlet and small speaker, defroster and door stop on the RHS	the RHS absorption material on the front and on the side rear doors removed
	Conf21	X	X	X	X	X	X		X		BUS OFF	A-post cord (as extra feature) Removed		extra tape on air inlet and small speaker, defroster and door stop on the RHS	the RHS absorption material on the front and on the side rear doors removed, on the rear all removed
	Conf22		X											extra tape on air inlet and small speaker, defroster and door stop on the RHS	RC
	Conf23		X											extra tape on air inlet and small speaker, defroster and door stop on the RHS	RC with tape on the mesh under the hood

Appendix C

Below is the Matlab code used in 3D Cam coherence analysis.

process_3D_Cam.m

```
[filename pathname]=uigetfile;
load(filename);
f=Coherence.x_values.start_value:Coherence.x_values.increment:(Cohere
nce.x_values.number_of_values-1)*Coherence.x_values.increment;
y=Coherence.y_values.values;
y=y(:,2:end); % Discard ir channel data
[y_maximum i_maximum]=maximum(y);
y_maximum_mean=mean(y_maximum); % mean coherence
f_maximum=f(i_maximum); %

out_filename=strcat(pwd,'\result_3D_Cam.xls');
if ~exist(out_filename)
      xlswrite(out_filename,{'f_maximum',
'mean_maximum_coherence','name'});
end

[~,~,raw]=xlsread(out_filename);
while mode(f_maximum)<=500
    f_maximum=f_maximum(f_maximum~=mode(f_maximum));
end
raw=[raw;{mode(f_maximum),y_maximum_mean,filename},]; % MOST FREQUENT
F_MAXIMUM IS STORED!!
xlswrite(out_filename,raw)
```